Simultaneous Detection of Ozone and Nitrogen Dioxide by Oxygen Anion Chemical Ionization Mass Spectrometry: A Fast Time Response Sensor Suitable for Eddy Covariance Measurements

Gordon A. Novak, Michael P. Vermeuel, Timothy H. Bertram

5   Department of Chemistry, University of Wisconsin – Madison, Madison, WI, USA

Correspondence to: Timothy H. Bertram (timothy.bertram@wisc.edu)

Abstract. We report on the development, characterization, and field deployment of a fast time response sensor for measuring ozone (O_3) and nitrogen dioxide (NO_2) concentrations utilizing chemical ionization time-of-flight mass spectrometry (CI-ToFMS) with oxygen anion (O_2^-) reagent ion chemistry. We demonstrate that the oxygen anion chemical ionization mass

10   spectrometer (Ox-CIMS) is highly sensitive to both O_3 (180 counts s^{-1} $pptv^{-1}$) and NO_2 (97 counts s^{-1} $pptv^{-1}$), corresponding to detection limits (3σ, 1 s averages) of 13 and 9.9 pptv, respectively. In both cases, the detection threshold is limited by the magnitude and variability in the background determination. The short-term precision (1 s averages) is better than 0.3% at 10 ppbv O_3 and 4% at 10 pptv NO_2. We demonstrate that the sensitivity of the O_3 measurement to fluctuations in ambient water vapor and carbon dioxide is negligible for typical conditions encountered in the troposphere. The application of the Ox-CIMS

15   to the measurement of O_3 vertical fluxes over the coastal ocean, via eddy covariance (EC), was tested during summer 2018 at Scripps Pier, La Jolla CA. The observed mean ozone deposition velocity ($v_d(O_3)$) was 0.013 cm s^{-1} with a campaign ensemble limit of detection (LOD) of 0.0027 cm s^{-1} at the 95% confidence level, from each 27-minute sampling period LOD. The campaign mean and one standard deviation range of O_3 mixing ratios were 41.2 ± 10.1 ppbv. Several fast ozone titration events from local NO emissions were sampled where unit conversion of O_3 to NO_2 was observed, highlighting instrument utility as a

20   total odd oxygen ($O_x = O_3 + NO_2$) sensor. The demonstrated precision, sensitivity, and time resolution of this instrument highlight its potential for direct measurements of O_3 ocean–atmosphere and biosphere–atmosphere exchange from both stationary and mobile sampling platforms.

1 Introduction

The deposition of O_3 to the ocean surface is a significant component of the tropospheric ozone budget. Global chemical

25   transport model studies that explicitly treat O_3 deposition, indicate that approximately one-third of total ozone dry deposition is to water surfaces (Ganzeveld et al., 2009). However, the magnitude of total annual global ozone deposition to ocean surfaces is highly sensitive to the deposition velocity parameterization used, with model estimates ranging from 95 to 360 Tg yr^{-1} (Ganzeveld et al., 2009; Luhar et al., 2017). Several common global chemical transport models including GEOS-Chem (Bey et al., 2001), MOZART-4 (Emmons et al., 2010), and CAM-chem (Lamarque et al., 2012) apply a globally uniform deposition

30   velocity (v_d) that ranges between 0.01–0.05 cm s^{-1} depending on the model. In comparison to terrestrial measurements, where

O_3 dry deposition velocities are relatively fast (>0.1 cm s^{-1}, (Zhang et al., 2003), there is a paucity of direct observations of ozone deposition to the ocean surface necessary to constrain atmospheric models. Previous studies of O_3 deposition to water surfaces have been made from coastal towers (Gallagher et al., 2001), aircraft (Faloona et al., 2005; Kawa and Pearson, 1989; Lenschow et al., 1981), underway research vessels (Helmig et al., 2012), and in the laboratory (McKay et al., 1992), with observed $v_d(O_3)$ ranging between 0.01 and 0.15 cm s^{-1}There is only one reported study of O_3 deposition to freshwater, which showed $v_d(O_3)$ of 0.01 cm s^{-1} (Wesely et al., 1981).. Measured deposition rates to snow and ice vary widely, with most observations of $v_d(O_3)$ from 0 to 0.2 cm s^{-1}, while models suggest $v_d(O_3)$ from 0 to 0.01 cm s^{-1} (Helmig et al., 2007). Reactions of O_3 with iodide and dissolved organic compounds (DOC) in the ocean are known to play a controlling role in setting $v_d(O_3)$ and may explain some of the variability in observations (Chang et al., 2004; Ganzeveld et al., 2009). However, these quantities have not typically been measured during field studies of $v_d(O_3)$. To date there is no consensus on whether measured ocean O_3 deposition velocities show a wind speed dependence (Fairall et al., 2007). The most comprehensive dataset is from Helmig et al., (2012), which reported a deposition velocity range of 0.009 – 0.034 cm s^{-1} from 1700 hours of observation over five research cruises. This dataset showed variability of $v_d(O_3)$ with wind speed (U_{10}) and sea–surface temperature (SST), highlighting the need for further field observations as constraints for model parameterizations.

The small magnitude of O_3 ocean–atmosphere vertical fluxes presents a significant analytical challenge for existing ozone sensors used in eddy covariance (EC) analyses. Driven in part by stringent sensor requirements for EC techniques, significant uncertainties in the magnitude and variability of ozone deposition to water surfaces remain. In contrast, O_3 vertical fluxes to terrestrial surfaces are 10 to 100 times faster than to water surfaces, significantly loosening sensor precision requirements. Nonetheless, significant variability in $v_d(O_3)$ exists between surface types (e.g. soil *vs.* leaf) (Wesely and Hicks, 2000). Terrestrial deposition velocities also show strong diel and seasonal variability due to factors such as stomatal opening and within-canopy chemistry (Fares et al., 2010; Fowler et al., 2001; Kurpius and Goldstein, 2003). Highly accurate and precise measurements of O_3 are required to correctly model the response of $v_d(O_3)$ to each of these factors. While terrestrial and ocean exchange studies have substantial differences in experimental design, a sensor suitable for ocean–atmosphere ozone deposition measurements *via* EC is expected to be highly capable of biosphere–atmosphere measurements due to the significantly larger deposition rates and similar accuracy requirements.

Eddy covariance measurements typically require fast (1-10 Hz), high precision sensors in order to resolve covariance on the timescales of the fastest atmospheric turbulent eddies. Due to this constraint, standard O_3 monitoring instruments which utilize UV-absorption detection do not have suitable time response or precision for EC measurements and ozone flux measurements have primarily utilized fast response chemiluminescence sensors. Chemiluminescence detectors can use either gas-phase, dry, or wet reagents for detection with important differences between them (Muller et al., 2010). Gas-phase chemiluminescence sensors are typically based on the reaction of O_3 with nitric oxide (NO) to form an excited state NO_2^* which then relaxes to the ground state, emitting a photon that can be detected. This method has well understood reaction kinetics and allows for high sensitivity detection on the order of 2.8 counts s^{-1} pptv^{-1} (Bariteau et al., 2010; Pearson, 1990). A practical disadvantage to this technique is the necessity of a compressed cylinder of NO which is highly toxic. Wet chemiluminescence

techniques are used less, as they exhibit generally lower sensitivity than dry chemiluminescence sensors and can be limited by issues in the liquid flow (Keronen et al., 2003).

Dry chemiluminescence sensors have the simplest operation and have seen the most regular use for EC studies (Güsten et al., 1992; Tuovinen et al., 2004). However, dry chemiluminescence sensor discs require conditioning with high ozone (up to 400 ppbv for several hours) before operation, are known to degrade over time, and have high variability in sensitivity between sensor discs (Weinheimer, 2007). These factors have led to limitations in long term stability and to uncertainty in calibration factors for dry chemiluminescence sensors, resulting in uncertainty in the accuracy of the flux measurement (Muller et al., 2010). Muller et al.(2010), also reported a comparison of two identical co-located dry chemiluminescence sensors with half-hourly flux values differing by up to a factor of two and a mean hourly flux difference ranging from 0 to 23% between sensors. Recently Zahn et al., (2012) reported the development of a commercial dry chemiluminescence ozone detector capable of fast (>10 Hz) measurements with high sensitivity ($\sim$9 counts s^{-1} pptv^{-1}) suitable for EC or mobile platform sampling. However, they also report issues of short- and long-term drift and variability between sensor discs. These accuracy and drift concerns have driven an interest in the development of a new, stable and fast ozone sensor suitable for EC measurements from both stationary and mobile sampling platforms.

In addition to the inherently small magnitude of $v_d(O_3)$, the fast chemical titration of O_3 by NO (R1) often complicates the interpretation of $v_d(O_3)$ measurements. Surface emissions of NO result in a high bias in the measured deposition velocity when the titration reaction (R1) is fast relative to the transport time to the height of the sensor.

$$O_3 + NO \rightarrow NO_2 + O_2 \qquad k(O_3+NO) = 1.8 \times 10^{-14} \text{ cm}^3 \text{ molecule}^{-1} \text{ s}^{-1} \qquad \text{(R1)}$$

Surface NO emissions from both biogenic and anthropogenic sources are widespread, with ocean emissions on the order of 1 $\times$ 10^8 molecules cm^{-2} s^{-1} (Zafiriou and McFarland, 1981) and soil emissions ranging from 5 $\times$ 10^9 to 2 $\times$ 10^{11} molecules cm^{-2} s^{-1} (Yienger and Levy, 2004). These emissions correspond to a positive bias in the observed $v_d(O_3)$ dry deposition rate on the order of 5% in the marine atmosphere (discussed in section 3.7.1) and up to 50% in a forested site (Dorsey et al., 2004). Simultaneous flux detection of O_3 with one or both of NO or NO_2 is commonly used to address this flux divergence problem (Finco et al., 2018; Stella et al., 2013). However, these studies typically require separate sensors for O_3 and NO$_x$ which can introduce additional sources of uncertainty. Related challenges of fast O_3 titration exists for quantification of O_3 from mobile platforms where there is dynamic sampling of different airmasses with potentially differing O_3–NO–NO_2 steady-state conditions.

In what follows, we describe the characterization and first field observations of a novel oxygen anion chemical ionization time-of-flight mass spectrometer (Ox-CIMS) sensor for O_3 and NO_2. Over the past two decades, chemical ionization mass spectrometry (CIMS) techniques have emerged as sensitive, selective, and accurate detection methods for a diverse suite of reactive trace gases (Huey, 2007). Successful application of CIMS for EC flux measurements have been demonstrated from many sampling platforms including ground sites (Kim et al., 2014; Nguyen et al., 2015), aircraft (Wolfe et al., 2015), and underway research vessels (Blomquist et al., 2010; Kim et al., 2017; Yang et al., 2013) employing a variety of reagent ion

chemistry systems. Here we demonstrate the suitability of the Ox-CIMS for EC flux measurements and provide detailed laboratory characterization of the instrument.

2 Laboratory Characterization

2.1 Chemical-ionization time-of-flight mass spectrometer

A complete description of the CI-ToFMS instrument (Aerodyne Research Inc., TOFWERK AG) can be found in Bertram et al. (2011). In what follows we highlight significant differences in the operation of the instrument from what is discussed in Bertram et al., (2011). Oxygen anions are generated by passing an 11:1 volumetric blend of Ultrahigh Purity (UHP) N_2 and O_2 gas (both Airgas 5.0 grade) through a polonium-210 α-particle source (NRD, P-2021 Ionizer). This N_2:O_2 volume ratio was found empirically to maximize total reagent ion signal in our instrument while minimizing background signal at the O_3 detection product (CO_3^-,– 60 m/Q). Further discussion of the reagent ion chemistry and precursor concentration can be found in sections 2.2 and 2.8. The reagent ion stream then mixes with ambient air in an ion-molecule reaction (IMR) chamber held at 95 mbar where product ions were generated. Further discussion of the dependence of instrument sensitivity on IMR pressure can be found in section 2.6. At this pressure, the residence time in the IMR is estimated to be on the order of 100 ms. Product ions then pass into three differentially pumped chambers before reaching the ToF mass analyzer. Ions first move from the IMR to a collisional dissociation chamber (CDC) held at 2 mbar which houses a short-segmented RF-only quadrupole ion guide. Field strengths in the IMR and CDC were tuned to be as soft as possible to preserve the transmission of weakly bound clusters while still maintaining acceptable total ion signals (ion optic potentials are listed in Table S1). Ions then sequentially pass into a second RF-only quadrupole chamber held at 1.4×10^{-2} mbar and a final chamber containing focusing optics which prepare the ion beam for entry into the compact ToF mass analyzer (CToF, TOFWERK AG and Aerodyne Research Inc.). The mass resolving power ($M/\Delta M$) of the instrument as configured for these experiments was greater than 900 at –60 m/Q. All ion count rates reported here are for unit mass resolution integrated peak areas. In this work extraction frequencies of 75 kHz were used, resulting in mass spectra from 27-327 –m/Q. All mass spectra were saved at 10 Hz for analysis.

2.2 Oxygen Anion Chemistry

Oxygen anion (O_2^-) reagent ion chemistry has been investigated previously for its use in the detection of nitric acid and more recently hydrogen peroxide (Huey, 1996; O'Sullivan et al., 2018; Vermeuel et al., 2019). Oxygen anion chemistry has also been used for chemical analysis of aerosol particles in a thermal desorption instrument, primarily for detection of particle sulfate and nitrate (Voisin et al., 2003). Oxygen anion chemistry has also been used for the detection of SO_2 *via* a multi-step ionization process where CO_3^- reagent ions are first generated by the reaction of O_2^- with added excess O_3 in the presence of CO_2. The CO_3^- reagent ion then ligand switches with SO_2 to form SO_3^- which then quickly reacts with ambient O_2 to form the

primary detected SO_5^- product (Porter et al., 2018; Thornton et al., 2002a). Ionization of analytes by oxygen anion reagent ion chemistry proceeds through both charge transfer (R2) and adduct formation (R3).

$$O_2(H_2O)_n^- + A \rightarrow O_2(H_2O)_n + A^- \tag{R2}$$

130 $$O_2(H_2O)_n^- + B \rightarrow B \cdot O_2(H_2O)_n^- \tag{R3}$$

It is expected that charge transfer from oxygen will occur to any analyte with an electron affinity (E.A.) greater than O_2 (0.45 eV, (Ervin et al., 2003)) resulting in a relatively non-specific reagent ion chemistry (see Rienstra-Kiracofe et al., (2002) for a compilation of molecular E.A. values).. Adduct formation is observed when the binding enthalpy of the adduct is larger than that of the oxygen-water adduct and the adduct is stable enough to be preserved through the ion optics. This adduct

135 formation framework is analogous to what has been shown for iodide reagent ion chemistry (Lee et al., 2014).

The O_2^- reagent ions present in the IMR are expected to have a series of attached water molecules at ambient humidity and the IMR pressure (95 mbar) and electric field strengths used in this study (Bork et al., 2011). The reagent ion is therefore reported as $O_2(H_2O)_n^-$ for the remainder of this work. In the recorded mass spectra from our instrument, all reagent ion signal is observed as $n = 0$–1 (i.e., O_2^- and $O_2(H_2O)^-$) as seen in Fig. 1. Oxygen anion-water clusters larger than $n = 1$ are likely present in the

140 IMR but H_2O evaporates off of the cluster in the CDC before detection due to the lower binding enthalpy of each additional water in $O_2(H_2O)_n^-$ (Bork et al., 2011) and the high filed strength at the exit of the CDC (Brophy and Farmer, 2016). Variability in the number of attached water molecules (n) as a function of humidity introduces the possibility of a water dependence on the ion chemistry, which is discussed further in Section 2.5.

The detection of ozone (O_3) by oxygen anion reagent ion chemistry proceeds *via* a two-step reaction leading to the

145 formation of a carbonate anion (CO_3^-), which is the final detected product. First, the oxygen anion ($O_2(H_2O)_n^-$) either transfers an electron to ozone forming O_3^- (R4a) or forms a stable cluster with ozone (R4b). The ozone anion (either bare or as a cluster with $O_2(H_2O)_n$) then reacts with a neutral CO_2 molecule to form CO_3^- (R5a–5b) which is the primary, detected product in the mass spectrometer. The electron affinity of O_3 is 2.1 eV (Arnold et al., 1994).

$$O_3 + O_2(H_2O)_n^- \rightarrow O_3^- + O_2 + nH_2O \tag{R4a}$$

150 $$O_3 + O_2(H_2O)_n^- \rightarrow O_2(O_3)(H_2O)_n^- \tag{R4b}$$

$$O_3^- + CO_2 \rightarrow CO_3^- + O_2 \tag{R5a}$$

$$O_2(O_3)(H_2O)_n^- + CO_2 \rightarrow CO_3^- + 2O_2 + nH_2O \tag{R5b}$$

It is not clear whether it is the bare ozone anion (R4a & R5a) or the cluster (R4b & R5b) that goes on to react with CO_2 to form the carbonate anion. The $O_2(O_3)(H_2O)_n^-$ product has not been observed in the mass spectrometer, but it may

155 exist in the IMR and dissociate as it transfers into the CDC prior to detection. A small amount of ozone is detected directly as O_3^- but the magnitude of this signal is less than 1% of the signal of CO_3^- during ambient sampling. The proposed mechanism of CO_3^- formation is supported by a study using isotopically labelled oxygen to form labelled ozone anions ($^{18}O_3^-$) in a corona discharge source which then reacted with CO_2 to form the detected product $C^{18}OO_2^-$ (Ewing and Waltman, 2010). This product supports that a single oxygen is transferred from the ozone anion to carbon dioxide (as in R5a).

160   The detection of NO_2 proceeds directly through a charge transfer reaction with $O_2(H_2O)_n^-$ to form the detected NO_2^- product (R6). This is expected based upon the high E.A. of NO_2 (2.27 eV, (Ervin et al., 1988)) compared to O_2 (E.A 0.45 eV).

$$NO_2 + O_2(H_2O)_n^- \rightarrow NO_2^- + O_2 + nH_2O \hspace{4cm} (R6)$$

      Oxygen anions are expected to be a highly general reagent ion chemistry, showing sensitivity to an array of analytes. While the focus of this work is on detection of O_3 and NO_2, detection of hydrogen peroxide, nitric acid, formic acid, sulfur

165 dioxide and other species with the Ox-CIMS has demonstrated good performance (Vermeuel et al., 2019). An example ambient mass spectrum recorded at 1 Hz sampling is shown in Fig. 1, with several major peaks highlighted. Also apparent are an abundance of peaks throughout the spectra with high signal intensity. During ambient observations, over one third of masses from $-m/Q$ 27-327 showed signal intensity greater than 1×10^4 counts per second (cps). A larger survey and classification of oxygen anion reagent ion chemistry to utilize this versatility is underway.

170 **2.3 Laboratory calibration**

Laboratory calibrations of the Ox-CIMS were performed to determine instrument sensitivity to O_3 and NO_2. Ozone was generated by passing UHP Zero Air (ZA, Airgas 5.0 grade) through a mercury lamp UV source (Jelight Co, Irvine CA). Outflow from the lamp source was diluted in UHP ZA and split between the Ox-CIMS and a factory calibrated 2B POM ozone monitor (2B Technologies) with an accuracy of $\pm$ 1.5 ppbv, which served as our reference standard. Ozone concentrations

175 were varied over the range 0–80 ppbv and instrument response was determined to generate a calibration curve. NO_2 was delivered from a certified standard cylinder (Scott-Marrin 4.84 $\pm$ 0.1 ppmv). The primary NO_2 standard was diluted in UHP ZA to span the range of 0–10 ppbv. Dilutions of calibration standards were made in UHP ZA which was humidified to the desired amount by splitting a portion of the flow through a bubbler containing 18 MΩ water. CO_2 (Airgas Bone Dry grade) was added to the dilution flow to maintain mixing ratios of 380 ppmv for all calibrations (See Section 2.6). A Vaisala HMP

180 110 sensor continuously measured relative humidity and temperature inline downstream of the Ox-CIMS and POM inlets. All flows were controlled by mass flow controllers (MKS instruments, 1179C series) with an estimated total uncertainty of 10%. Example calibration curves for O_3 and NO_2 are shown in Fig. 2. An overview of instrument sensitivity, limits of detection (LOD), and precision to O_3 and NO_2 is given in Table 1.

2.4 Absolute sensitivity

185 The absolute sensitivity of the Ox-CIMS for detection of analytes is controlled by the kinetics and thermodynamics of the reagent ion chemistry and the total ion generation and transmission efficiency of the instrument. Under the operational configuration described in Section 2.1, typical reagent ion signal ($O_2^- + O_2(H_2O)_n^-$) ranged from 0.8 to 2.2×10^7 counts s^{-1} (Fig. S1). The mean total reagent ion signal over 6 weeks of ambient sampling (Section 3.1) was 1.45×10^7 cps. The absolute instrument sensitivity at this reagent ion signal to O_3 and NO_2 is 180 and 97 cps pptv^{-1} respectively (at 8 g kg^{-1} SH). Total

190 instrument count rate is a complex function of instrument design, instrument ion optics tuning, Po-210 source decay, micro channel plate (MCP) detector decay, and ToF extraction frequency; all of which are either tunable parameters or vary in time.

Conversely, the reagent ion charge transfer or adduct formation chemistry for a given analyte sets a fundamental limit on sensitivity for a given instrument configuration. Sensitivity values can be normalized by scaling all signals to a fixed total reagent ion signal of 1×10^6 cps to isolate the sensitivity component controlled by reagent ion chemistry, separate from changes in instrument performance due to decay in the ion source or other factors. The total reagent ion signal is taken as the sum of the O_2^- and $O_2(H_2O)^-$ signals. Sensitivity values through the remainder of the text are reported as either absolute sensitivities in counts per second (cps pptv^{-1}) or normalized sensitivities in normalized counts per second (ncps pptv^{-1}). Absolute sensitivity values control instrument limits of detection (LOD) and precision, while normalized sensitivities are used for comparison of calibration factors.

2.5 Dependence of instrument sensitivity on specific humidity

The dependence of instrument sensitivity on ambient water content was assessed for specific humidity (SH) ranging between 0–16 g kg^{-1} (approximately 0-80% RH at 25 °C) by triplicate calibrations as shown in Fig. 3. Sensitivity to O_3 had no significant dependence on specific humidity over the range 4-16 g kg$^-$. Sensitivity to NO_2 has a specific humidity dependence over the range 4–16 g kg^{-1}, decreasing from 7.9 to 4.6 ncps pptv^{-1}. A 30% and 45% decline in sensitivity was observed from 0 to 4 g kg^{-1} for O_3 and NO_2 respectively. This low humidity range is rarely sampled in the boundary layer over water surfaces but may be significant in some terrestrial or airborne deployments and would require careful calibration. The SH range from 8 to 16 g kg^{-1} corresponds to approximately 40 to 80% RH at 25 °C which is typical of the humidity range over mid-latitude oceans (Liu et al., 1991). *Ab initio* calculations of $O_2^-(H_2O)_n$ and $O_3^-(H_2O)_n$ clusters performed by Bork et al. (2011) showed that charge transfer from the bare (n=0) O_2^- to O_3 was exothermic at ca. -160 kJ/mol. At larger cluster sizes of $n = 4–12$, charge transfer becomes less favorable and converges to ca. -110 kJ/mol. An increase in n from 0 to 4 over the SH range 0–4 g kg^{-1} is a potential explanation for the initial decline in sensitivity observed with SH before levelling off from 4–16 g kg^{-1}. It is not known if the enthalpy of charge transfer from $O_2^-(H_2O)_n$ to NO_2 follows a similar trend with n. Ion mobility studies to determine the $O_2^-(H_2O)_n$ cluster size with SH and IMR pressure would provide valuable insight on the observed dependence of sensitivity on water content.

2.6 Dependence on CO₂

The ionization pathway for detection of O_3 with $O_2^-(H_2O)_n$ reagent ion chemistry differs from typical chemical ionization schemes, in that it involves a two-step reaction of charge transfer to ozone forming O_3^-, which then reacts with CO_2 to form the detected CO_3^- product (R4-R5). Therefore, we assessed the impact of CO_2 mixing ratio in the sample flow on O_3 sensitivity as shown in Fig. 4. Calibration curves were generated by diluting ozone in dry UHP N_2 and mixing in a flow of variable CO_2 (Airgas, Bone Dry Grade) mixing ratios before sampling. At nominally 0 ppmv CO_2, the O_3^- ionization product (–48 m/Q) was detected with sensitivity of 14 ± 2 ncps pptv^{-1} and the CO_3^- product (–60 m/Q) at 5 ± 1 ncps pptv^{-1}. For CO_2 mixing ratios from 60 to 500 ppmv, the O_3^- signal is less than 1% of the CO_3^- product and the sensitivity at the CO_3^- product is independent of CO_2

within the uncertainty. The presence of a significant fraction (36%) of the CO_3^- product with nominally 0 ppmv CO_2 suggests the presence of a slight leak rate of CO_2 *via* diffusion through the perfluoroalkoxy alkane (PFA) tubing, or CO_2 contamination in the UHP N_2 supply. The manufacturer stated upper limit of CO_2 in the UHP N_2 is 1 ppmv which we take to be the lower limit achievable in our system. A CO_2 mixing ratio of only 1 ppmv is still an order of magnitude excess relative to a high end ambient O_3 mixing ratio of 100 ppbv. An exponential fit of the O_3^- product *vs* CO_2 indicates that O_3^- makes up less than 1% of the detected ozone at CO_2 mixing ratios greater than 10 ppmv. This suggests ambient samples will always have a substantial excess of CO_2 necessary to drive the reaction completely to the CO_3^- product. The measured flat response from 60–500 ppmv CO_2 indicates that natural variability in ambient CO_2 will have negligible impact on ambient measurements of ozone. No other analytes that we have calibrated for with the Ox-CIMS (HCOOH, HNO_3, H_2O_2) have shown a CO_2 mixing ratio dependence, suggesting that CO_2 may be uniquely involved in the detection of O_3 and is not a general feature of the oxygen-anion chemistry. All other reported laboratory calibrations reported here were performed at CO_2 mixing ratios of 380 ppmv and all reported sensitivities are for the CO_3^- product. This CO_2 dependence also requires careful consideration during instrument background determinations by UHP N_2 overflow which is discussed in Section 2.8.

2.7 Dependence on IMR pressure

Instrument sensitivity to O_3 increases with increasing IMR pressure as shown in Fig. 5. The normalized signal of O_3 increases by 60% at an IMR pressure of 95 mbar compared to 70 mbar when sampling a constant O_3 source of 35 ppbv. IMR pressure was increased in approximately 5 mbar steps, with CDC pressure held constant at 2 mbar, and a three-minute dwell time at each step to ensure signal and pressure were stabilized. Total reagent ion signal did not change significantly over this pressure range. Pressures above 95 mbar were not investigated due to concerns over corresponding increases in CDC pressure with the pinhole and pumping configuration used in this work. There is no evident plateauing in the signal increase over the IMR pressure range investigated here, indicating that further optimization is likely possible by operating at higher IMR pressures. The increase in sensitivity with IMR pressure could be fit well with an exponential least squares fit, which is plotted in Fig.5. The physical meaning of the exponential relationship is not clear. The source of the response of sensitivity to pressure is not definitive but can possibly be attributed to the increase in the total number of collisions during the 100 ms residence time in the IMR and the corresponding weakening of those collisions. Higher collisional frequencies also lead to proportionally weaker collisions which could better preserve a weakly bound $O_2(O_3)(H_2O)_n^-$ cluster and allow a longer lifetime to react with CO_2 before dissociation. The operational IMR pressure of 95 mbar used here was empirically selected to maximize sensitivity to O_3 without increasing CDC pressure beyond the desired range. Investigation of higher IMR pressures, up to the operation of an atmospheric pressure interface, has the potential to further increase the instrument sensitivity to O_3.

2.8 Instrument background and limits of detection

Instrument backgrounds were assessed by periodically overflowing the inlet with UHP N_2 during field sampling. Details of the inlet and zeroing conditions used are discussed further in Section 3.1. During N_2 overflow, O_3 displayed a consistently

255   elevated background on the order of 3.1×10^5 cps corresponding to 2.1×10^4 ncps, or approximately 1.3 ppbv O_3, at a typical total reagent ion signal of 1.45×10^7 cps. A representative background determination is shown in Fig. 6. The magnitude of the O_3 background was observed to vary with the O_2:N_2 ratio in the reagent ion precursor flow when sampling a UHP ZA overflow with 380ppm CO_2 as shown in Fig. S2. The background O_3 count rate was observed to increase from 3.0×10^4 to 6.3×10^4 ncps as the O_2 volume fraction in the reagent ion delivery gas flow (f_{O2}) was increased from 0.05 to 0.4. The dependence of

260   the background O_3 signal on f_{O_2} suggests that the observed background O_3 is formed directly in the alpha ion source and is not from off-gassing of inlet and instrument surfaces. The magnitude of this background O_3 does not vary when sampling UHP zero air or N_2, further confirming that the background O_3 is formed directly in the ion source from the O_2 used to generate the reagent ion. An operational f_{O_2} of 0.08 (actual volumetric flow ratio O_2:N_2 of 200:2200 sccm) was selected to balance maximizing the total reagent ion signal while minimizing the O_3 ion-source background (3.1×10^5 cps). The magnitude of this

265   O_3 background was observed to be highly consistent during field sampling at a constant f_{O_2} of 0.08 and well resolved from all ambient observations (Fig. S3). The 1σ deviation of the distribution of normalized adjacent differences of O_3 signal during background periods gives an upper limit of variability of 9% between adjacent background periods. A variability of 9% corresponds to a difference of 70 pptv between subsequent O_3 background determinations. The magnitude of this O_3 background is a fundamental limit on the achievable limit of detection.

270   Because CO_2 was not added to the UHP N_2 overflow during field sampling, the reaction was not driven fully to the CO_3^- product and some O_3^- signal at $-m/Q$ 48 was observed during UHP N_2 overflow periods as shown in Fig. S4. The magnitude of the O_3 signal observed as O_3^- was approximately 55% of the CO_3^- product (mean 1.2×10^4 and 9.6×10^3 ncps respectively) during overflow periods. The total sensitivity to O_3 as the sum of the O_3^- and CO_3^- was observed to be constant as a function of CO_2 as shown in Fig. 4. We therefore assign equal sensitivity to each O_3 detection product and took the sum

275   of signal at O_3^- and CO_3^- in order to determine the total background O_3 concentration. This issue will be corrected in future deployments by the addition of CO_2 to the N_2 overflow used for backgrounds which will drive the product fully to CO_3^-. The mean background of O_3 for the full field sampling period was 1.3 ± 0.3 ppbv. The 10 Hz precision of O_3 during an individual N_2 overflow period was found to be 0.75%, corresponding to 7.5 pptv as shown in Fig. S5. This suggests that variability in the O_3 signal from this background source is constant over short timescales and has a negligible impact on instrument precision

280   during ambient sampling.

          The 10 Hz limit of detection for O_3 is 42 pptv for a S/N of 3, and a mean background O_3 signal of 2.1×10^4 ncps as calculated using Eq. 1, below from Bertram et al., 2011, where C_f is the calibration factor, $[x]$ is the analyte mixing ratio, t is averaging time in seconds, and B is the background count rate. The optimum LOD from the minimum of the Allan variance at an 11 second averaging time is 4.0 pptv (Fig. S6a).

285    $$\frac{S}{N} = \frac{C_f[X]t}{\sqrt{C_f[X]t - 2Bt}} \qquad\qquad\qquad E1$$

The mean background signal during field sampling for NO_2 was 3.5 x 10^3 ncps which corresponds to 0.28 ppbv. At this background level, the 10 Hz LOD for NO_2 is 26 pptv for a S/N of 3. The optimum LOD for NO_2 is 2.3 pptv at an averaging time of 19 seconds, determined from the minimum of the Allan variance (Fig. S6b). The background signal of NO_2 is notably above zero indicating either off gassing from inlet walls or a secondary production of NO_2 in the instrument. A possible source of this background is from degradation of other species such as nitric acid or alkyl nitrates on the inlet walls. Additional calibration will be necessary to ensure that observed NO_2 signal is not a secondary product of other species and we can currently quantify their potential interference on measured NO_2.

2.9 Reagent ion saturation and secondary ion chemistry

During ambient sampling the ozone signal (as CO_3^- detected at -60 m/Q) is of comparable magnitude to the O_2^- reagent ion signal as shown in Fig. 1. High analyte concentrations (> 5 ppbv) have been shown previously to result in non-linear calibration curves for unnormalized signals (Bertram et al., 2011; Veres et al., 2008). In our system we do not observe non-linearity in the normalized O_3 calibration for our highest concentration calibration point of 80 ppbv despite the CO_3^- signal being larger than the O_2^- reagent ion (9 x 10^6 cps and 6 x 10^6 cps respectively). The electron affinity (E.A.) of carbonate is from 3.26 (Hunton et al., 1985) to >3.34 eV (Snodgrass et al., 1990) and is significantly higher than that of oxygen (E.A. 0.45 eV), making it unlikely that carbonate is involved in charge transfer reactions when excess O_2^- is present. . At high O_3 concentrations, the reagent ion signal magnitude is reduced, which necessitates normalizing sensitivities to the 1 x 10^6 cps of reagent ion signal before quantification. For NO_2 (E.A. 2.27 eV), the normalized sensitivity showed no dependence on O_3 concentrations from 0 to 80 ppbv. Carbonate reagent ion chemistry has been utilized for detection of HNO_3 and H_2O_2 *via* adduct formation raising additional concern about potential secondary ion chemistry (Reiner et al., 1998). In laboratory calibrations, shown in Fig. S7, introduction of 0 to 40 ppb H_2O_2 resulted in the titration of the O_3 signal of 0.06 ppbv per ppbv H_2O_2. H_2O_2 was detected as an adduct with O_2^- and not CO_3^-, indicating that O_2^- reagent ion chemistry is more favorable despite high CO_3^- signal intensity. The Ox-CIMS O_3 measurement also compared well (R^2 =0.99) against an EPA AQS O_3 monitor over 1 month of ambient sampling where H_2O_2 and HNO_3 concentrations both exceeded 5 ppbv at times (see Section 3.1 for further discussion of field intercomparison), further supporting the CO_3^- detection product as a robust indicator of O_3 in complex sampling environments.

Ab initio calculations of the binding enthalpies of O_2^- and CO_3^- reagent ions with H_2O, HNO_3, H_2O_2, and CH_3OOH were performed with the MP2/aug-cc-pvdz-PP theory and basis set in order to assess the relative favorability of adduct formation between O_2^- and CO_3^- Adduct formation with O_2^- was favorable relative to CO_3^- by 2.5 to 17 kcal mol^{-1} for all analytes that were calculated. All calculated binding enthalpy values are listed in Table S2.

2.10 Short- and long- term precision

Short term precision of the instrument was assessed by calculating the normalized difference between adjacent 10 Hz data points over a 27-minute sampling period of a constant ambient analyte concentration *via* Eq. 2.

$$NAD = \frac{[X]_n - [X]_{n-1}}{\sqrt{[X]_n [X]_{n-1}}} \qquad\qquad\qquad E2$$

The standard deviation of the Gaussian fit of the distribution of normalized adjacent differences (NAD) is a direct measure of the short-term instrument precision (Bertram et al., 2011). The 1σ precision from the NAD distribution for 10 Hz sampling of 38 ppbv ozone is 0.74% (Fig. 7). The 10 Hz precision for sampling of 2.3 ppbv NO_2 is 1.1% The short-term precision for both analytes was larger than expected if the noise was driven by counting noise alone (10 Hz counting noise limit for O_3 and NO_2 at the concentrations used above are 0.12% and 0.63% respectively), indicating that other potential points of optimization in the instrument configuration are required to further improve short-term precision. Notably, the observed noise source appears to be white noise given the Gaussian distribution of the NAD (Thornton et al., 2002b).

Short term precision was assessed as a function of count rate by calculating the NAD for all masses in the spectrum over a stable 27-minute sampling period for both 1 Hz and 10 Hz data averaging. From this assessment, precision was observed to improve approximately linearly in a log-log scaling for count rates between 1 x 10^3 and 1 x 10^6 cps (Fig. S8) as expected in the case where counting noise drives instrument precision. Above 1 x 10^6 cps there is an apparent asymptote where precision no longer improves with count rate. The counting noise limited 10 Hz precision for 10^6 and 10^7 cps are 0.32% and 0.1% respectively, while the measured values were 0.75 and 2%. The counting noise limited precision is calculated as $\sqrt{N}/N$ where N is the number of counts during the integration time. This precision limit could be driven by an uncharacterized source of white noise in the instrument, including MFC drift, IMR turbulence, ion optic voltage drift, and pump drift. Measurement precision of O_3 and NO_2 could be improved by a factor of 5 and 2 respectively if this non-counting noise source of white noise was eliminated.

In theory, detection limits can be improved by signal averaging to a lower time resolution than the 10 Hz save rate. Signal–to–noise ratios are expected to improve with the square root of the integration time. At longer timescales, factors including instrument drift become significant, creating a limit on the upper end of averaging time which optimizes signal–to–noise. This was assessed quantitatively by calculation of the Allan variance as shown in Fig. S6 (Werle et al., 1993).

3 Field results and discussion

3.1 Ozone field calibration and intercomparison

Performance of the Ox-CIMS was compared against a co-located EPA Air Quality System (AQS) O_3 monitor (Thermo-Fisher 49i, AQS ID 17-097-1007) over one month of ambient sampling during the Lake Michigan Ozone Study 2017 (LMOS 2017) in Zion, IL (Vermeuel et al., 2019). A regression analysis between the two instruments at one-minute averaging showed strong agreement ($R^2 = 0.99$) as shown in Fig. 8. Ox-CIMS concentrations were averaged to 1 ppbv bins which was the output data resolution of the EPA data logger system for the (Thermo-Fisher 49i). Error bars are the 1σ standard deviation of each Ox-CIMS bin average. Near one–to–one agreement (slope of 0.99) between instruments lends confidence to the calibration,

baselining, and long-term stability of the Ox-CIMS. The Ox-CIMS was located on the roof of a trailer (approx. 5 m above ground) and sampled through a 0.7 m long, 0.925 cm i.d., PFA inlet. The inlet was pumped at flow rate of 18-20 slpm from

350   which the Ox-CIMS subsampled at 1.5 slpm. Temperature and RH were recorded inline downstream of the subsampling point. The Ox-CIMS sampling point was approximately 10 m horizontally from the Thermo-Fisher 49i and both instruments sampled at approximately equal heights. Instrument backgrounds of the Ox-CIMS were determined every 70 minutes by overflowing the inlet with dry UHP N_2. Calibration factors were determined by the in-field continuous addition of a C-13 isotopically labelled formic acid standard to the tip of the inlet. Laboratory calibrations of the Ox-CIMS to formic acid and O_3 as a function

355   of specific humidity were determined immediately pre- and post-campaign and were used to calculate a humidity dependent sensitivity of O_3 relative to formic acid. That relative sensitivity was then used to determine the in-field sensitivity to O_3 by scaling field sensitivities of formic acid from the continuous additions. Full details of this deployment and calibration methods are described in Vermeuel et al., (2019). The EPA O_3 monitor shows a persistent high bias at low O_3 concentrations (<10 ppbv) relative to the Ox-CIMS. This discrepancy could arise from known interferences from water, mercury, and other species in

360   254 nm UV absorbance detection of ozone (Kleindienst et al., 1993).

3.2 Eddy covariance experiment overview

The Ox-CIMS was deployed to the 330 m long Ellen Browning Scripps Memorial Pier (hereon referred to as Scripps Pier) at the Scripps Institute of Oceanography (32° 52.0' N, 117° 15.4' W) during July and August 2018 for EC measurements of O_3 vertical fluxes. This site has been used regularly for EC flux observations from our group and others (Ikawa and Oechel, 2015;

365   Kim et al., 2014; Porter et al., 2018). The Ox-CIMS was housed in a temperature-controlled trailer at the end of the pier. The Ox-CIMS sampled from a 20 m long PFA inlet manifold with the intake point co-located with a Gil-Sonic HS-50 sonic anemometer which recorded 3-dimensional winds sampling at 10 Hz. The Ox-CIMS inlet and sonic anemometer were mounted on a 6.1 m long boom that extended beyond the end of the pier to minimize flow distortions. The inlet height was 13 m above the mean lower low tide level. The Ox-CIMS inlet was located 8 cm below the sonic anemometer with a 0 cm horizontal

370   displacement. The inlet manifold consisted of a 0.64 cm i.d. sampling line, a 0.64 cm i.d. overflow line, and a 0.47 cm i.d. calibration line all made of PFA. The inlet sample line was pumped at 18-23 slpm (Reynolds number 3860-4940) by a dry scroll pump (SH-110, Agilent) to ensure a fast time response and maintain turbulent flow. Flow rates in the inlet sample line were recorded by a mass flow meter but were not actively controlled. The inlet manifold, including calibration and overflow lines, was held at 40 °C *via* a single resistively coupled circuit along the length of the manifold and controlled by a PID

375   controller (Omega, model CNi 16). The Ox-CIMS front block and IMR were held at 35 °C. The Ox-CIMS subsampled 1.5 slpm from this inlet manifold through a critical orifice into the IMR. Ambient humidity and temperature were also recorded in-line downstream of the subsampling point.

3.2.1 Calibration

Instrument sensitivity was assessed by the standard addition of a C–13 isotopically labelled formic acid standard for 3 minutes every 35 minutes at the ambient end of the inlet manifold. Ozone mixing ratios were determined by scaling the humidity dependent sensitivity of O_3 from pre- and post-campaign calibrations to the field calibrations of C–13 formic acid. Ambient O_3 was also measured at 10 s time-resolution with a 2B technologies Personal Ozone Monitor (POM). The POM had a separate 10 m long, 0.47 cm i.d. PFA sampling line located 12 m from the Ox-CIMS inlet manifold and sonic anemometer. The POM was used as an independent verification of the Ox-CIMS measurement and was not used for calibration.

3.2.2 Backgrounds and inlet residence time

Instrument backgrounds were determined every 35 minutes by overflowing the entire inlet manifold with dry UHP N_2. Background and ambient count rates were first converted to concentrations using the laboratory determined humidity dependent sensitivities for O_3 and NO_2 scaled to the C-13 formic acid standard addition sensitivity. Background concentrations of O_3 and NO_2 from before and after each 30-minute ambient sampling period were interpolated over the ambient sampling period which was then subtracted from each 10 Hz concentration data point to obtain a background corrected time-series. Background concentrations of O_3 had a mean 1.5 ppbv and a drift of 1% between adjacent background periods, determined by the distribution of the NAD of the mean background concentrations.

The signal response of O_3 during dry N_2 overflows were fit to an exponential decay function to characterize inlet gas response times (Ellis et al., 2010). Best fit estimates for decay time constants for O_3 across overflow periods were from 0.2 to 0.44 seconds. NO_2 decay responses were fit to a bi-exponential decay to characterize inlet evacuation time (τ_1) and wall interaction times (τ_2) (Ellis et al., 2010). τ_2 for NO_2 was determined to be approximately 3.2 s. This suggests a potential interference at the NO_2 peak, as NO_2 is expected to have minimal wall equilibration, similar to O_3. NO_2 also shows a continually elevated signal during overflow periods suggesting off gassing from inlet or instrument surfaces. The cause of this slow NO_2 decay and elevated background is not clear but could be from degradation of nitric acid or nitrate containing aerosol on the instrument surfaces.

The instrument response time (τ_r) for O_3 can be calculated during zeroing periods as the time required for the signal to fall to 1/e of its initial value. The response time of the instrument was calculated for each overflow period during field sampling, with a mean value of 0.28 s. The cutoff frequency (f_{cut}) of the instrument is defined as the frequency where the signal is attenuated by a factor of $1/\sqrt{2}$ (Bariteau et al., 2010). The cutoff frequency can also be calculated from τ_r according to Eq. 3.

$$f_{cut} = \frac{1}{2\pi \, \tau_r} \hspace{6cm} \text{E3}$$

The calculated f_{cut} from the measured mean response time was 0.57 Hz. This value suggests that minimal attenuation in the flux signal (cospectra) should be apparent at frequencies less than 0.57 Hz. The instrument response time and thus cutoff frequency are function of the flow rate and sampling line volume. The flow rate of 18-23 slpm was the maximum achievable

410   with the tubing and pumping configuration used here but could be improved in future to minimize tubing interactions and shift
f_{cut} towards higher frequencies.

3.2.3 Eddy covariance flux method

The transfer of trace gases across the air−sea interface is a complex function of both atmospheric and oceanic processes, where
gas exchange is controlled by turbulence in the atmospheric and water boundary layers, molecular diffusion in the interfacial

415   regions surrounding the air−water interface, and the solubility and chemical reactivity of the gas in the molecular sublayer.
The flux (F) of trace gas across the interface is described by Eq. 4, as a function of both the gas-phase (C_g) and liquid phase
(C_l) concentrations and the dimensionless gas over liquid Henry's law constant (H), where K_t, the total transfer velocity for
the gas (with units cm s^{-1}), encompasses all of the chemical and physical processes that govern air−sea gas exchange. Surface
chemical reactivity terms to the gas exchange rate are incorporated into the K_t term.

420   $$F = -K_t\left(C_g - HC_l\right) \hspace{4cm} \text{E4}$$

Trace gas flux (F) can be measured with the well-established eddy covariance (EC) technique where flux is defined
as the time average of the instantaneous covariances from the mean of vertical wind (w) and the scalar magnitude (here O$_3$)
shown in Eq. 5. Overbars are means and primes are the instantaneous variance from the mean. Here N is the total number of
10 Hz data points during the 27-minute flux averaging period.

425   $$F = \frac{1}{N}\sum_{i=1}^{N}(w_i - \overline{w})\left(O_{3,i} - \overline{O_3}\right) = \langle w'O_3'\rangle \hspace{3cm} \text{E5}$$

$$v_d = \frac{F}{\overline{C_g}} \hspace{5cm} \text{E6}$$

For purely depositing species where the water side concentration is negligible, C_l and H can be neglected in Eq. 4 and K_t can
be reformulated into a deposition velocity (v_d) calculated according to Eq. 6, where $\overline{C_g}$ is the mean gas phase mixing ratio
during the flux averaging period. A summary of concentration and flux results for the full deployment period are given in

430   Table 2.

3.3 General Data Corrections

Several standard eddy covariance data filters and quality control checks were applied before analysis. General filters included:
1.) Wind sector: Only periods of mean onshore flow (true wind direction 200-360°) were used.
2.) Friction velocity: A friction velocity (U_*) threshold was applied to reject periods of low shear driven turbulence (Barr

435   et al., 2013) described further below.
3.) Stationarity: Each 27-minute flux period was divided into five even non-overlapping subperiods. Flux periods were
rejected if any of the subperiods differed by more than 40% (Foken and Wichura, 1996).

The applied U_* filter was determined by comparing the observed U_* values to U_* calculated with the NOAA COARE bulk
flux v 3.6 algorithm (Fairall et al., 2011). COARE U_* were calculated using measured meterology including wind speed, sea-

surface temperature, air temperature, and relative humidity. Flux periods were rejected if the observed U_* differed from the calculated U_* by more than 50%. The stress relationship of wind-speed to U_* is well understood over the ocean. Fixed U_* filters of *ca.* 0.2 m s^{-1} are used frequently as a default in terrestrial flux studies but would reject nearly all observation periods in this study. The observed friction velocities are consistent with other marine flux studies where surface roughness lengths are significantly smaller than over terrestrial surfaces (Porter et al., 2018). Methods of determining site specific U_* thresholds typically require long-term data series which were not available here (Papale et al., 2006). Papale et al., (2006), applied a minimum U_* threshold of 0.1 m s^{-1} for forest sites and 0.01 m s^{-1} for short vegetation sites where typical U_* values are lower. The selected U_* filter rejects an additional 44% of the flux periods remaining after the wind direction filter.. The stationarity criteria rejected a further 100 flux periods, potentially driven by periods of activity on the pier driving changes in the sampled O_3. Outliers in $v_d(O_3)$ and the flux limit of detection were determined and removed for points three scaled median absolute deviations from the median. This outlier filter removed an additional 16 data points. After the wind direction filter and all quality control filters were applied, 73% of flux periods were rejected leaving 246 quality-controlled flux periods. Eddy covariance flux values were calculated using 27-minute time windows. The O_3 timeseries was detrended with a linear function prior to the flux calculation. The O_3 and vertical wind data were despiked using a mean absolute deviation filter before the eddy covariance flux calculation following Mauder et al., (2013).

3.3.1 Planar Fit Wind Coordinate Rotation

Coordinate rotation of the *u*, *v*, and *w* wind components was performed by the planar fit method to remove unintentional tilts in the sonic mounting and account for local flow distortions (Wilczak et al., 2001). Briefly, the mean *u*, *v*, and *w* wind components and the stress tensor were determined for each 15-minute onshore flow period during the full campaign. A linear regression was used to find the best fit of a plane with a coordinate system where the z-axis is perpendicular to the mean streamline. Individual 27-minute flux periods are then rotated such that the x-axis is along the mean wind and $\bar{v} = 0$. Vertical wind velocity ($\bar{w}$) in any individual rotation period may be non-zero due to mesoscale motions but $\bar{w}$ for the full campaign is zero. The residual mean vertical velocity in any individual rotation period is subtracted out, so it does not impact the Reynolds averaging.

3.3.2 Lag time shift

The Ox-CIMS signal is delayed relative to the sonic anemometer due to transit time in the inlet line which must be accounted for before calculating the covariance between the vertical wind and analyte concentration. The cross-covariance of the two timeseries were first calculated within a ± 5 s window to determine the lag time of the Ox-CIMS and synchronize with the anemometer. The volumetric evacuation time of the inlet is 1.65 to 2.1 s for the inlet volume and flow rates of 18 to 23 slpm used in this study. Following the method and terminology outlined in Langford et al., (2015), the position of the maximum (MAX) of the cross-covariance is taken as the lag time needed to align the vertical wind and analyte concentration for that flux period. A representative lag time determination with a larger lag window (± 10 s) using the MAX method is shown in Fig. 10.

In low signal-to-noise (SNR) data, the use of the MAX leads to high variability in the determined lag time caused by uncertainty in the position of the peak in the cross-covariance. This results in a systematic high bias on the absolute magnitude of the resulting flux. The position of the maximum of a centered running median (AVG) function of the cross-covariance is an alternative method to determine lag time with less expected bias for low SNR data (Langford et al., 2015; Taipale et al., 2010). Lag times for each O_3 flux period determined by the MAX and a 10 point AVG method showed reasonable agreement, with a campaign average lag time from the MAX with a mean of 1.0 seconds and the AVG at 0.7 seconds (Fig. S9). This agreement suggests that a clear peak in the cross-covariance was present for most flux periods leading to a convergence of the two methods. This lag time also shows agreement with the inlet response time of 0.9 s determined during dry N_2 overflows. Due to the convergence of the determined lag times around a central value, a prescribed lag time of 0.9 s was used for all reported $v_d(O_3)$ values. A prescribed lag time has the least bias to extreme values caused by noise, provided that the true lag time is known well (Langford et al., 2015). Deposition velocities were then recalculated with the prescribed lag time of 0.9 s and with the MAX and AVG method over a narrower lag window of $\pm\ 3$ which is expected to be physically reasonable range for the flow rate and inlet line volume. The mean $v_d(O_3)$ using the prescribed, MAX, and AVG lag times were 0.013, 0.012, and 0.012 cm s^{-1} respectively, suggesting the campaign mean value was relatively insensitive to the lag time method.

3.4 Cospectra and Ogives

The frequency weighted cospectrum of O_3' with w' has a well characterized form with exhibited dependence on wind-speed and measuring height (Kaimal et al., 1972). Comparison of observed cospectra shape against the idealized Kaimal cospectra is useful to validate that the observed signal was not significantly attenuated at low or high frequencies. Cospectral averaging is performed by binning frequency into 50 evenly log spaced bins and normalizing the integrated cospectra to 1. The integral of the unnormalized cospectra is the flux for that observation period. The mean wind-speed binned cospectra of sensible heat and O_3 appear to match well with the idealized Kaimal cospectra for an unstable boundary layer at sampling height $z = 13m$ (Fig.11).

The ogive is the normalized cumulative distribution of the cospectra, which is used to validate both that no high-frequency attenuation is present and that the flux averaging time is sufficiently long that all frequencies contributing for the flux is captured. Figure 11 shows the averaged cospectra and ogives for O_3 and sensible heat flux from the average of two flux averaging periods 14:10 – 15:20 on July 20th. The asymptote to 1 at low frequencies validates that the 27-minute flux averaging time was sufficiently long for this site to capture the largest flux carrying eddies. High pumping rates in sampling line ensured that turbulent flow was always maintained in the line (Reynolds number 3860-4940). Higher Reynolds numbers in the turbulent regime lead to smaller high frequency attenuation (Massman, 1991). The overlap of the idealized Kaimal curve and the observed sensible heat and O_3 ogives suggest that high frequency attenuation in the sampling line is minimal above approximately 0.4 Hz, consistent with our calculated f_{cut} of 0.57 Hz. We calculate the high frequency correction transfer function for turbulent attenuation in a tube from Massman, (1991) as a constraint, which is shown in Fig. 11b. This transfer

505   function shows attenuation primarily above 1 Hz and is not sufficient to describe the observed attenuation above 0.4 Hz. This implies that the attenuation observed cannot be explained only as turbulent smearing in the inlet and that other wall interactions are likely present.

Due to the small magnitude of the O_3 EC flux there is low signal to noise in the cospectra at high frequency for many of the flux averaging periods. This makes application of cospectra based correction factors challenging and likely to introduce added

510   variance on the signal. We therefore apply an attenuation correction factor following Bariteau et al., (2010). First we calculate the idealized unattenuated Kaimal cospectra (C_{wx_k}) (Eq. 7) for each flux period, and then apply frequency attenuation to that cospectra by applying a low-pass filter function ($H(f)$) characterized by τ_c (Eq. 8). The ratio of the flux of the unattenuated (F_{raw}) and attenuated (F_{att}) cospectra is then taken as the correction factor (A_f, Eq.9) to apply to the observed O_3 flux (Eq. 10). Where n is the surface layer normalized frequency defined as $n = f\,z/U$, where z is the measurement height and U is the

515   horizontal wind speed. $F_{O_3,corr}$ is the attenuation corrected O_3 flux and $F_{O_3,obs}$ is the original measured flux. This approach has the benefit of applying a single correction factor to the total flux, rather than frequency dependent corrections which might serve to amplify noise at high frequencies. The net impact of this correction factor was an increase of campaign mean $v_d(O_3)$ of 4%.

520    $$C_{wx\_k} = \frac{11n}{(1+11.3n)^{7/4}} \qquad\qquad\qquad \text{E7.}$$

$$H(f) = [1 + (2\pi f \tau_c)^2]^{-1} \qquad\qquad\qquad \text{E8.}$$

$$A_f = \frac{F_{raw}}{F_{att}} \frac{\int_0^{fn} C_{wx_k}(f)\,df}{\int_0^{fn} C_{wx_k}(f)\,[H(f)]^{1/2}\,df} \qquad\qquad\qquad \text{E9.}$$

$$F_{O_3,corr} = A_f F_{O_3,obs} \qquad\qquad\qquad \text{E10.}$$

525   We also calculate the attenuated flux from the model of Horst, (1997) shown in Eq. 11, for a response time (τ_c) of 0.0.28 s, and a wind speed of 3 m s^{-1} to be 6%. The general agreement of the Horst and Bariteau attenuation correction factors indicate that the applied correction is reasonable.

$$\frac{F_m}{F_x} = \frac{1}{1+(2\pi n_m \tau_c U/z)^\alpha} \qquad\qquad\qquad \text{E11}$$

Where F_m/F_x is the ratio of the measured flux to the unattenuated flux, U is wind speed, z is measurement height, and n_m and

530   α are scaling factors for an unstable boundary layer taken as 0.085 and 7/8 respectively.

3.5 Uncertainty and flux limit of detection

Variance in the atmospheric O_3 signal was estimated by calculating the autocovariance of the signal during a 27-minute flux averaging period (Fig. S11). Uncorrelated white noise only contributes to the first point in the autocovariance spectrum, while autocovariance at longer time shifts represents real atmospheric variance or correlated instrument drift (Blomquist et al., 2010;

535   Langford et al., 2015). For the analysed period, white noise is typically 45 to 65% of the total variance and atmospheric variance is 35 to 55%. This corresponds to a standard deviation from white noise $\sigma_{O_3, noise}$ of 0.4 ppbv.

The error in each flux averaging period (LOD_σ) can be determined by taking the standard deviation of the cross-covariance between vertical wind speed and mass spectrometer signal at lag times significantly longer than the calculated true lag time
540   (Spirig et al., 2005; Wienhold et al., 1995). The random flux error is determined using lag windows of -150 to -180 and 150 to 180 s, which are significantly larger than the true lag time from sensor separation of 0.9 s as shown in Figure S12. The selection of the -150 to -180 and 150 to 180 s lag windows is somewhat arbitrary and may still capture organized atmospheric structure that persists over long time periods. We also calculate the root mean squared deviation (LOD_{RMSE}) of the cross-covariance over the same lag windows as proposed by Langford et al., (2015), which captures the variance in the cross-
545   covariance in those regions but also accounts for long term offsets from zero in the cross-covariance. The resulting error from the LOD_σ and LOD_{RMSE} methods showed good correlation (Fig S13), with periods where the LOD_{RMSE} error is larger. We apply the RMSE method for our reported flux error determination. The final deposition velocity limit of detection was determined for each 27-minute flux averaging period by multiplying the LOD_{RMSE} error by 1.96 to give the flux limit-of-detection at the 95% confidence level. The flux error was then divided by the mean O_3 concentration for that averaging period
550   to convert from flux to deposition velocity units. The campaign ensemble flux LOD_{RMSE} was 0.0027 cm s^{-1}, calculated using Eq. 12 following Langford et al.,(2015). A total of 59 out of 246 (24%) flux periods had deposition velocities below the campaign ensemble LOD. These values are still included in the reported mean $v_d(O_3)$.

$$\overline{LOD} = \frac{1}{N}\sum_{i=1}^{N} LOD^2 \qquad\qquad\qquad\qquad\qquad\qquad\qquad E12$$

3.6 Density fluctuation corrections

555   The Ox-CIMS measures O_3 as the apparent mixing ratio relative to moist air, as is true of all CIMS based measurements, which means fluctuations in the density of air due to changes in temperature, pressure, and humidity could introduce a bias in the EC flux measurement (Webb et al., 1980). The temperature and pressure in the Ox-CIMS and sampling lines were both actively controlled during sampling, making density fluctuations from those sources negligible. The long (20 m) inlet sampling line used likely also dampened a substantial portion of the water vapor flux. This has been demonstrated in an EC study utilizing
560   a closed path H_2O sensor for EC flux measurements (through an 18 m long, 0.635 cm i.d. inlet, pumped at 18 slpm, comparable to the inlet used in this study) which showed complete attenuation above 0.1 Hz and overall attenuation of ~80% of the H_2O (latent heat) flux (Yang et al., 2016). However, without a direct measure of water vapor fluctuations collocated with the Ox-CIMS this is difficult to definitively rule out in our measurement. We therefore calculate a conservative estimate of this correction factor from Eq 45b. in Webb et al., (1980), assuming a latent heat flux of 50 W m^{-2} and neglecting the sensible heat
565   term which is removed by active heating of the inlet. For a specific humidity of 12 g kg^{-1}, a temperature of 293 K, a pressure of 1 atm, and an O_3 mixing ratio of 40 ppbv, we calculate a flux correction term of 2.6 x 10^9 molecules cm^{-2} s^{-1}, which is 20%

of our mean measured flux of -1.3 x 10^{10} molecules cm^{-2} s^{-1}. We expect that the actual density correction for our instrument much smaller given that water vapor fluctuations were likely dampened in the inlet line, and the high latent heat flux used in the calculation (50 W m^{-2}). Due to the uncertainty in this correction term for our instrument, we do not add it to our measured

570   flux values and instead use the calculated value above as a conservative constraint on the magnitude. The addition of a Nafion drier on the inlet has been successfully implemented in other O_3 flux instruments to fully remove water fluctuations and will be used in future deployments of the Ox-CIMS (Bariteau et al., 2010).

3.7 Flux divergence

3.7.1 Surface NO emissions

575   The observed dry deposition velocity of ozone is potentially biased by simultaneous air-sea exchange of nitric oxide (NO). NO is expected to be emitted from the ocean on the order of 1 x 10^8 molecules cm^{-2} s^{-1} with dependence on dissolved surface nitrate and solar irradiance (Zafiriou and McFarland, 1981). This NO source near the surface will cause titration of O_3 to NO_2 resulting in a positive bias for the observed $v_d(O_3)$. Assuming a maximum NO emission flux of 5 x 10^8 molecules cm^{-2} s^{-1} and that all NO reacts with O_3 before being advected to the sensor height, the resulting O_3 flux bias would be -5 x 10^8 molecules

580   cm^{-2} s^{-1}. Our mean case of 40 ppbv O_3 and $v_d (O_3)$ of 0.013 cm s^{-1} corresponds to a flux of -1.3 x 10^{10} molecules cm^{-2} s^{-1}. Therefore, the resulting bias in observed $v_d(O_3)$ from NO emissions is 3.8% or 4.9 x 10^{-4} cm s^{-1}. This value is an upper limit for expected ocean NO emissions and is well within the uncertainty of the observed $v_d(O_3)$. There is also potential for short term anthropogenic emissions of NO (such as from a boat engine passing by the sensor) to create a flux divergence term. We expect that the combination of signal despiking and the flux stationarity criteria described in Section 3.3 will minimize the

585   impact of this potential divergence term. Despiking will remove most short term (<1 s) emission events and the stationarity criteria will filter out any period where longer term titration events cause large changes in the observed flux within a flux measurement period.

3.7.2 Free troposphere entrainment

The entrainment of O_3 enhanced or depleted air in the free troposphere to the marine boundary layer (MBL) creates a potential

590   flux gradient that will contribute to the measured flux values at the near surface measurement height (z_o) of 13 m. Lenschow et al., (1982) presented aircraft observations of O_3 deposition over the Gulf of Mexico at heights of 15, 60, and 325 m which showed a strong flux gradient term driven by entrainment from the free troposphere. The boundary layer height (z_i) during those flights was approximately 1.2 km, suggests a strong flux gradient was present even within the surface layer (approximated as the lowest 10% of the boundary layer). The magnitude of this flux gradient depends on the magnitude of the

595   O_3 concentration gradient (ΔC) and the entrainment velocity (w_e) of air from free troposphere into the MBL. Faloona et al., (2005), reported entrainment velocities from 0.12 to 0.72 cm s^{-1} and an enhancement in O_3 (ΔC) of 20 ppbv in the free troposphere relative to the boundary layer in the summertime eastern subtropical pacific. Using those values and Equations

13and 14 below we calculate the percent fractional error from entrainment on the observed flux for a range of reasonable ΔC and w_e as shown in Fig. 12 (Blomquist et al., 2010).

$$\frac{\Delta F_{0,est}}{F_0} = \frac{z}{z_i}\left(\frac{F_i}{F_0} - 1\right) \tag{E13}$$

$$F_i = w_e \Delta C \tag{E14}$$

Where z_i is the boundary layer height, z is the measurement height, and F_i and F_0 are the entrainment flux and surface flux respectively. We use the SIO measurement height (z) = 13 m and mean surface flux (F_o) = -5.2 x 10^{-3} ppbv m s^{-1} (from v_d = 0.013 cm s^{-1} and [O$_3$] = 40 ppbv), and an O$_3$ mixing ratio gradient (ΔC) from -20 to +20 ppbv in the free troposphere relative to the boundary layer. The resulting fractional error in our observed mean surface flux from Scripps Pier using the values from Faloona et al, 2005 (ΔC of +20 ppbv, MBL height of 800m) is 4.4% for w_e of 0.12 and 33% for 0.72 cm s^{-1}. This entrainment flux error is clearly significant for marine O$_3$ flux measurements assuming there is a gradient of O$_3$ in the free troposphere relative to boundary layer. This entrainment flux error is independent of the surface flux instrument measurement error and adds a systematic bias on the surface flux measurement. This calculation also makes clear that marine O$_3$ measurements should be made as close to the surface as possible, and that the O$_3$ concentration gradient and entrainment rate should be explicitly measured if possible. We do not have an explicit measure of ΔC, w_e, or the MBL height so we tentatively assign entrainment error of up to 33% from the maximum values of those parameters reported in Faloona et al. (2005). We emphasize this source of uncertainty is independent of the O$_3$ sensor and is a systematic bias that should be considered in all O$_3$ air-sea exchange determinations.

4 Fast NO$_2$ measurements, eddy covariance and O$_3$ titration

Discussion of EC flux results have been limited to O$_3$ because ocean—atmosphere exchange of NO$_2$ is expected to be small and below the limit of detection of our instrument. The potential flux divergence from the reaction of O$_3$ with NO is also below the instrument flux limit of detection as discussed in section 3.6. However, over terrestrial surfaces where NO$_2$ emissions can be large, we expect this instrument would be well suited for measuring NO$_2$ flux. From Equations 15 and 16, following Bariteau et al., (2010) and Lenschow and Kristensen, (1985), we calculate the we calculate an expected flux LOD for the case where counting noise is the controlling term in the flux error. The calculated flux LOD is 4.3 x 10^9 molecules cm s^{-2} s^{-1} (1.6 pptv m s^{-1}) for an NO$_2$ mixing ratio of 1 ppbv and a friction velocity of 0.2 m s^{-1}.

$$F = C_a\sqrt{\frac{0.06u_*^2}{C_a\xi\Gamma}} \tag{E15.}$$

$$\Gamma = \frac{a\,z}{U} \tag{E16}$$

Where u_* is the friction velocity (m s^{-1}), C_a is the gas phase concentration (ppbv), ξ is the instrument sensitivity (cps ppbv^{-1}), and Γ is the integral time scale (s). Γ can be further expressed following Eq. 12 where a is constant taken as 0.3 for neutral

conditions (Lenschow and Kristensen, 1985), z is the measurement height (here 10 m), and U is the horizontal wind speed at that measurement height (taken as 5 m s^{-1}).

630   Observations of a short duration NO plume from a boat motor starting near our inlet at Scripps Pier highlights the utility of the simultaneous O_3 and NO_2 detection from this instrument (Fig. 13). Highly localized NO emissions were observed as the titration of O_3 and prompt production of NO_2. Observed total odd oxygen ($O_x = O_3 + NO_2$) was conserved during this titration event, where NO_2 and O_3 concentrations were determined from independent calibration factors and backgrounds. The 1:1 conversion of O_x from O_3 to NO_2 shown in Fig. 13b, validates the laboratory generated instrument calibration factors for
635   O_3 and NO_2. The temporal agreement of the O_3 and NO_2 signals also demonstrates that both O_3 and NO_2 are transmitted through the inlet and detected with nearly identical instrument response times. This analysis assumes that there were no direct NO_2 emissions during the titration event. A NO_2 to NO_x emission ratio of 0.08 was observed for ship emissions from diesel motors on inland shipping vessels (Kurtenbach et al., 2016). Without additional knowledge amount the NO_x emission source during this event, the observed conservation of total O_x could be partially driven by compensating errors within 10%. This
640   simultaneous detection of both O_x species is likely also well suited for mobile sampling in the presence of dynamic NO emission sources, which challenge other fast ozone measurements. This method would also be well suited for direct measurement of flux divergence in the presence of strong surface NO emission sources.

5 Conclusions and Outlook

This study demonstrated the utility of oxygen anion chemical ionization mass spectrometry for the fast and sensitive detection
645   of O_3 and NO_2. Field measurements of O_3 dry deposition to the ocean surface from Scripps Pier, La Jolla CA demonstrate that this method has suitable time response, precision, and stability for successful EC measurements. The mean measured $v_d(O_3)$ with the Ox-CIMS is in within range ofprior studies of O_3 ocean-atmosphere exchange. Further optimization and characterization of the Ox-CIMS is ongoing, including efforts to validate the specificity of the NO_2 detection, addition of a Nafion drier system, and better background determination methods. While this work has focused primarily on the deposition
650   of O_3 to the ocean surface, the demonstrated instrument performance suggests the Ox-CIMS to be highly capable of O_3 and NO_2 flux measurements in the terrestrial biosphere and urban environments and from mobile platforms.

Author Contributions

GAN, MPV, and THB designed the lab and field experiments and GAN and MPV collected all data. GAN lead the data processing, interpretation and analysis with MPV contributing. GAN prepared the manuscript with contributions from all co-
655   authors. THB supervised all work and contributed to data analysis, writing and editing of the manuscript.

Acknowledgments

This work was supported by National Science Foundation (NSF) Grant GEO AGS 1829667.

The authors thank the staff at Scripps Pier, Scripps Institute of Oceanography and at the UW—Madison Department of Limnology for support in instrument deployments.

660   Glenn M. Wolfe is gratefully acknowledged for publicly providing a Matlab based "FluxToolbox" of analysis scripts, portions of which were altered for use in this analysis. Code is archived at https://github.com/AirChem

This research was performed using the computing resources and assistance of the UW-Madison Center for High Throughput Computing (CHTC) in the Department of Computer Sciences. The CHTC is supported by UW-Madison, the Advanced Computing Initiative, the Wisconsin Alumni Research Foundation, the Wisconsin Institutes for Discovery, and the National

665   Science Foundation, and is an active member of the Open Science Grid, which is supported by the National Science Foundation and the U.S. Department of Energy's Office of Science.

Competing Interests

The authors declare that they have no conflict of interest.

670   **Data Availability**

Scripps Pier ozone flux data will be made available at https://minds.wisconsin.edu/handle/1793/76304 following final publication. Other detail is available upon reasonable request to the corresponding author.

675

References

Arnold, D. W., Xu, C., Kim, E. H. and Neumark, D. M.: Study of low-lying electronic states of ozone by anion photoelectron spectroscopy of O 3-, J. Chem. Phys., 101(2), 912–922, doi:10.1063/1.467745, 1994.

680   Bariteau, L., Helmig, D., Fairall, C. W., Hare, J. E., Hueber, J. and Lang, E. K.: Determination of oceanic ozone deposition by ship-borne eddy covariance flux measurements, Atmos. Meas. Tech., 3(2), 441–455, doi:10.5194/amt-3-441-2010, 2010.

Barr, A. G., Richardson, A. D., Hollinger, D. Y., Papale, D., Arain, M. A., Black, T. A., Bohrer, G., Dragoni, D., Fischer, M. L., Gu, L., Law, B. E., Margolis, H. A., Mccaughey, J. H., Munger, J. W., Oechel, W. and Schaeffer, K.: Use of change-point

detection for friction-velocity threshold evaluation in eddy-covariance studies, Agric. For. Meteorol., 171–172, 31–45,
685   doi:10.1016/j.agrformet.2012.11.023, 2013.

Bertram, T. H., Kimmel, J. R., Crisp, T. A., Ryder, O. S., Yatavelli, R. L. N., Thornton, J. A., Cubison, M. J., Gonin, M. and
Worsnop, D. R.: A field-deployable, chemical ionization time-of-flight mass spectrometer, Atmos. Meas. Tech., 4(7), 1471–
1479, doi:10.5194/amt-4-1471-2011, 2011.

Bey, I., Jacob, D. J., Yantosca, R. M., Logan, J. A., Field, B. D., Fiore, A. M., Li, Q., Liu, H. Y., Mickley, L. J. and Schultz,
690   M. G.: Global modeling of tropospheric chemistry with assimilated meteorology: Model description and evaluation, J.
Geophys. Res. Atmos., doi:10.1029/2001JD000807, 2001.

Blomquist, B. W., Huebert, B. J., Fairall, C. W. and Faloona, I. C.: Determining the sea-air flux of dimethylsulfide by eddy
correlation using mass spectrometry, Atmos. Meas. Tech., 3(1), 1–20, doi:10.5194/amt-3-1-2010, 2010.

Bork, N., Kurtén, T., Enghoff, M. B., Pedersen, J. O. P., Mikkelsen, K. V. and Svensmark, H.: Ab initio studies of O - 2 (H
695   2O) n and O - 3 (H 2O) n anionic molecular clusters, ≤12, Atmos. Chem. Phys., 11(14), 7133–7142, doi:10.5194/acp-11-7133-
2011, 2011.

Brophy, P. and Farmer, D. K.: Clustering, methodology, and mechanistic insights into acetate chemical ionization using high-
resolution time-of-flight mass spectrometry, Atmos. Meas. Tech., 9(8), 3969–3986, doi:10.5194/amt-9-3969-2016, 2016.

Chang, W., Heikes, B. G. and Lee, M.: Ozone deposition to the sea surface: Chemical enhancement and wind speed
700   dependence, Atmos. Environ., 38(7), 1053–1059, doi:10.1016/j.atmosenv.2003.10.050, 2004.

Dorsey, J. R., Duyzer, J. H., Gallagher, M. W., Coe, H., Pilegaard, K., Weststrate, J. H., Jensen, N. O. and Walton, S.: Oxidized
nitrogen and ozone interaction with forests. I : Experimental observations and analysis of exchange with Douglas fir, Q. J. R.
Meteorol. Soc., doi:10.1256/qj.03.124, 2004.

Ellis, R. a, Murphy, J. G., Pattey, E., Haarlem, R. Van and Brien, J. M. O.: Characterizing a Quantum Cascade Tunable Infrared
705   Laser Di ff erential Absorption Spectrometer (QC-TILDAS) for measurements of atmospheric ammonia, Atmos. Meas. Tech.,
(x), 3309–3338, 2010.

Emmons, L., Lamarque, J., Hess, P. G. and Pfister, G.: Impact of Mexico City on Regional Air Quality from MOZART-4
simulations and MILAGRO observations, Atmos. Chem. Phys. Discuss., 10, 3457–3498, 2010.

Ervin, K. M., Ho, J. and Lineberger, W. C.: Ultraviolet photoelectron spectrum of nitrite anion, J. Phys. Chem., 92(19), 5405–
710   5412, doi:10.1021/j100330a017, 1988.

Ervin, K. M., Anusiewicz, I., Skurski, P., Simons, J. and Lineberger, W. C.: The only stable state of O2- is the X 2∏g ground
state and it (still!) has an adiabatic electron detachment energy of 0.45 eV, J. Phys. Chem. A, 107(41), 8521–8529,
doi:10.1021/jp0357323, 2003.

Ewing, R. G. and Waltman, M. J.: Production and utilization of CO3 - produced by a corona discharge in air for atmospheric
715   pressure chemical ionization, Int. J. Mass Spectrom., 296(1–3), 53–58, doi:10.1016/j.ijms.2010.08.024, 2010.

Fairall, C. W., Helmig, D., Ganzeveld, L. and Hare, J.: Water-side turbulence enhancement of ozone deposition to the ocean,
Atmos. Chem. Phys., 7(2), 443–451, doi:10.5194/acp-7-443-2007, 2007.

Fairall, C. W., Yang, M., Bariteau, L., Edson, J. B., Helmig, D., McGillis, W., Pezoa, S., Hare, J. E., Huebert, B. and Blomquist, B.: Implementation of the Coupled Ocean-Atmosphere Response Experiment flux algorithm with CO2, dimethyl sulfide, and O3, J. Geophys. Res. Ocean., 116(10), doi:10.1029/2010JC006884, 2011.

Faloona, I., Lenschow, D. H., Campos, T., Stevens, B., van Zanten, M., Blomquist, B., Thornton, D., Bandy, A. and Gerber, H.: Observations of Entrainment in Eastern Pacific Marine Stratocumulus Using Three Conserved Scalars, J. Atmos. Sci., 62(9), 3268–3285, doi:10.1175/JAS3541.1, 2005.

Fares, S., McKay, M., Holzinger, R. and Goldstein, A. H.: Ozone fluxes in a Pinus ponderosa ecosystem are dominated by non-stomatal processes: Evidence from long-term continuous measurements, Agric. For. Meteorol., 150(3), 420–431, doi:10.1016/j.agrformet.2010.01.007, 2010.

Finco, A., Coyle, M., Nemitz, E., Marzuoli, R., Chiesa, M., Loubet, B., Fares, S., Diaz-Pines, E., Gasche, R. and Gerosa, G.: Characterization of ozone deposition to a mixed oak-hornbeam forest - Flux measurements at five levels above and inside the canopy and their interactions with nitric oxide, Atmos. Chem. Phys., 18(24), 17945–17961, doi:10.5194/acp-18-17945-2018, 2018.

Foken, T. and Wichura, B.: Tools for quality assessment of surface-based flux measurements, Agric. For. Meteorol., 78(1–2), 83–105, doi:10.1016/0168-1923(95)02248-1, 1996.

Fowler, D., Flechard, C., Cape, J. N., Storeton-West, R. L. and Coyle, M.: Measurements of ozone deposition to vegetation quantifying the flux, the stomatal and non-stomatal components, Water. Air. Soil Pollut., doi:10.1023/A:1012243317471, 2001.

Gallagher, M. W., Beswick, K. M. and Coe, H.: Ozone deposition to coastal waters, Q. J. R. Meteorol. Soc., 127(572), 539–558, doi:10.1256/smsqj.57214, 2001.

Ganzeveld, L., Helmig, D., Fairall, C. W., Hare, J. and Pozzer, A.: Atmosphere-ocean ozone exchange: A global modeling study of biogeochemical, atmospheric, and waterside turbulence dependencies, Global Biogeochem. Cycles, 23(4), 1–16, doi:10.1029/2008GB003301, 2009.

Güsten, H., Heinrich, G., Schmidt, R. W. H. and Schurath, U.: A novel ozone sensor for direct eddy flux measurements, J. Atmos. Chem., 14(1–4), 73–84, doi:10.1007/BF00115224, 1992.

Helmig, D., Ganzeveld, L., Butler, T. and Oltmans, S. J.: The role of ozone atmosphere-snow gas exchange on polar, boundary-layer tropospheric ozone - A review and sensitivity analysis, Atmos. Chem. Phys., 7(1), 15–30, doi:10.5194/acp-7-15-2007, 2007.

Helmig, D., Lang, E. K., Bariteau, L., Boylan, P., Fairall, C. W., Ganzeveld, L., Hare, J., Huebert, B. J. and Pallandt, M.: Atmosphere-ocean ozone fluxes during the TexAQS 2006, STRATUS 2006, GOMECC 2007, GasEx 2008, and AMMA 2008 cruises, J. Geophys. Res. Atmos., 117(D4), doi:10.1029/2011JD015955, 2012.

Horst, T. W.: A simple formula for attenuation of eddy fluxes measured with first-order-response scalar sensors, Boundary-Layer Meteorol., 82(2), 219–233, doi:10.1023/A:1000229130034, 1997.

Huey, L. G.: The kinetics of the reaction of Cl-, O-, and O2- with HNO3: implications for measurements of HNO3 in the

atmosphere, Int. J. Mass Spectrom., 153, 145–150, 1996.

Hunton, D. E., Hofmann, M., Lindeman, T. G. and Castleman, A. W.: Photodissociation dynamics of CO3-, , 82(1), 134–150, 1985.

755 Ikawa, H. and Oechel, W. C.: Temporal variations in air-sea CO2 exchange near large kelp beds near San Diego, California, J. Geophys. Res. Ocean., 120(1), 50–63, doi:10.1002/2014JC010229, 2015.

Kaimal, J. C., Wyngaard, J. C., Izumi, Y. and Coté, O. R.: Spectral characteristics of surface-layer turbulence, Q. J. R. Meteorol. Soc., 98(417), 563–589, doi:10.1002/qj.49709841707, 1972.

Kawa, S. R. and Pearson, R.: Ozone budgets from the dynamics and chemistry of marine stratocumulus experiment, J.
760 Geophys. Res., 94(D7), 9809–9817, doi:10.1029/JD094iD07p09809, 1989.

Keronen, P., Reissell, A., Rannik, Ü.̈, Pohja, T., Siivola, E., Hiltunen, V., Hari, P., Kulmala, M. and Vesala, T.: Ozone flux measurements over a Scots pine forest using eddy covariance method: Performance evaluation and comparison with flux-profile method, Boreal Environ. Res., 8(4), 425–443, 2003.

Kim, M. J., Farmer, D. K. and Bertram, T. H.: A controlling role for the air-sea interface in the chemical processing of reactive
765 nitrogen in the coastal marine boundary layer, Proc Natl Acad Sci U S A, 111(11), 3943–3948, doi:10.1073/pnas.1318694111, 2014.

Kim, M. J., Novak, G. A., Zoerb, M. C., Yang, M., Blomquist, B. W., Huebert, B. J., Cappa, C. D. and Bertram, T. H.: Air-Sea exchange of biogenic volatile organic compounds and the impact on aerosol particle size distributions, Geophys. Res. Lett., 44(8), 3887–3896, doi:10.1002/2017GL072975, 2017.

770 Kleindienst, T. E., Hudgens, E. E., Smith, D. F., McElroy, F. F. and Bufalini, J. J.: Comparison of chemiluminescence and ultraviolet ozone monitor responses in the presence of humidity and photochemical pollutants, Air Waste, 43(2), 213–222, doi:10.1080/1073161X.1993.10467128, 1993.

Kurpius, M. R. and Goldstein, A. H.: Gas-phase chemistry dominates O3 loss to a forest, implying a source of aerosols and hydroxyl radicals to the atmosphere, Geophys. Res. Lett., doi:10.1029/2002GL016785, 2003.

775 Kurtenbach, R., Vaupel, K., Kleffmann, J., Klenk, U., Schmidt, E. and Wiesen, P.: Emissions of NO, NO2 and PM from inland shipping, Atmos. Chem. Phys., 16(22), 14285–14295, doi:10.5194/acp-16-14285-2016, 2016.

Lamarque, J. F., Emmons, L. K., Hess, P. G., Kinnison, D. E., Tilmes, S., Vitt, F., Heald, C. L., Holland, E. A., Lauritzen, P. H., Neu, J., Orlando, J. J., Rasch, P. J. and Tyndall, G. K.: CAM-chem: Description and evaluation of interactive atmospheric chemistry in the Community Earth System Model, Geosci. Model Dev., 5(2), 369–411, doi:10.5194/gmd-5-369-2012, 2012.

780 Langford, B., Acton, W., Ammann, C., Valach, A. and Nemitz, E.: Eddy-covariance data with low signal-to-noise ratio: Time-lag determination, uncertainties and limit of detection, Atmos. Meas. Tech., 8(10), 4197–4213, doi:10.5194/amt-8-4197-2015, 2015.

Lenschow, D. H. and Kristensen, L.: Uncorrelated Noise in Turbulence Measurements, J. Atmos. Ocean. Technol., 2, 68–81, doi:https://doi.org/10.1175/1520-0426(1985)002<0068:UNITM>2.0.CO;2, 1985.

785 Lenschow, D. H., Pearson, R. and Stankov, B. B.: Estimating the ozone budget in the boundary layer by use of aircraft

measurements of ozone eddy flux and mean concentration, J. Geophys. Res., 86(C8), 7291, doi:10.1029/JC086iC08p07291, 1981.

Lenschow, D. H., Pearson, R. J. and Stankov, B. B.: Measurements of Ozone Vertical Flux to Ocean and Forest, J. Geophys. Res., 87(C11), 8833–8837, doi:10.1029/JC087iC11p08833, 1982.

790   Liu, W. T., Tang, W. and Niler, P. P.: Humidity Profiles over the Ocean, J. Clim., 4(10), 1023–1034, 1991.

Luhar, A. K., Galbally, I. E., Woodhouse, M. T. and Thatcher, M.: An improved parameterisation of ozone dry deposition to the ocean and its impact in a global climate-chemistry model, Atmos. Chem. Phys., 17(5), 3749–3767, doi:10.5194/acp-17-3749-2017, 2017.

Massman, W. J.: The attenuation of concentration fluctuations in turbulent flow through a tube, J. Geophys. Res. Atmos.,
795   96(D8), 15269–15273, doi:10.1029/91JD01514, 1991.

McKay, W. A., Stephens, B. A. and Dollard, G. J.: Laboratory measurements of ozone deposition to sea water and other saline solutions, Atmos. Environ. Part A, Gen. Top., doi:10.1016/0960-1686(92)90467-Y, 1992.

Muller, J. B. A., Percival, C. J., Gallagher, M. W., Fowler, D., Coyle, M. and Nemitz, E.: Sources of uncertainty in eddy covariance ozone flux measurements made by dry chemiluminescence fast response analysers, Atmos. Meas. Tech., 3(1), 163–
800   176, doi:10.5194/amt-3-163-2010, 2010.

Nguyen, T. B., Crounse, J. D., Teng, A. P., St. Clair, J. M., Paulot, F., Wolfe, G. M. and Wennberg, P. O.: Rapid deposition of oxidized biogenic compounds to a temperate forest, Proc. Natl. Acad. Sci., 112(5), E392–E401, doi:10.1073/pnas.1418702112, 2015.

O'Sullivan, D. W., Silwal, I. K. C., McNeill, A. S., Treadaway, V. and Heikes, B. G.: Quantification of gas phase hydrogen
805   peroxide and methyl peroxide in ambient air: Using atmospheric pressure chemical ionization mass spectrometry with O2−, and O2−(CO2) reagent ions, Int. J. Mass Spectrom., doi:10.1016/j.ijms.2017.11.015, 2018.

Papale, D., Reichstein, M., Aubinet, M., Canfora, E., Bernhofer, C., Kutsch, W., Longdoz, B., Rambal, S., Valentini, R., Vesala, T. and Yakir, D.: Towards a standardized processing of Net Ecosystem Exchange measured with eddy covariance technique: Algorithms and uncertainty estimation, Biogeosciences, 3(4), 571–583, doi:10.5194/bg-3-571-2006, 2006.

810   Pearson, R.: Measuring ambient ozone with high sensitivity and bandwidth, Rev. Sci. Instrum., 61(2), 907–916, doi:10.1063/1.1141462, 1990.

Porter, J. G., De Bruyn, W. and Saltzman, E. S.: Eddy flux measurements of sulfur dioxide deposition to the sea surface, Atmos. Chem. Phys., 18(20), 15291–15305, doi:10.5194/acp-18-15291-2018, 2018.

Reiner, T., Möhler, O. and Arnold, F.: Improved atmospheric trace gas measurements with an aircraft-based tandem mass
815   spectrometer: Ion identification by mass-selected fragmentation studies, J. Geophys. Res. Atmos., 103(D23), 31309–31320, doi:10.1029/1998JD100003, 1998.

Rienstra-Kiracofe, J. C., Tschumper, G. S., Schaefer, H. F., Nandi, S. and Ellison, G. B.: Atomic and molecular electron affinities: Photoelectron experiments and theoretical computations, Chem. Rev., 102(1), 231–282, doi:10.1021/cr990044u, 2002.

820 Snodgrass, J. T., Roehl, C. M., Van Koppen, P. A. M., Palke, W. E. and Bowers, M. T.: Photodissociation of CO3-: Product kinetic energy measurements as a probe of excited state potential surfaces and dissociation dynamics, J. Chem. Phys., 92(10), 5935–5943, doi:10.1063/1.458363, 1990.

Spirig, C., Neftel, A., Ammann, C., Dommen, J., Grabmer, W., Thielmann, A., Schaub, A., Beauchamp, J., Wisthaler, A. and Hansel, A.: Eddy covariance flux measurements of biogenic VOCs during ECHO 2003 using proton transfer reaction mass

825 spectrometry, Atmos. Chem. Phys., 5, 465–481, doi:10.5194/acp-5-465-2005, 2005.

Stella, P., Kortner, M., Ammann, C., Foken, T., Meixner, F. X. and Trebs, I.: Measurements of nitrogen oxides and ozone fluxes by eddy covariance at a meadow: Evidence for an internal leaf resistance to NO2, Biogeosciences, doi:10.5194/bg-10-5997-2013, 2013.

Taipale, R., Ruuskanen, T. M. and Rinne, J.: Lag time determination in DEC measurements with PTR-MS, Atmos. Meas.

830 Tech., doi:10.5194/amt-3-853-2010, 2010.

Thornton, D. C., Bandy, A. R., Tu, F. H., Blomquist, B. W., Mitchell, G. M., Nadler, W. and Lenschow, D. H.: Fast airborne sulfur dioxide measurements by Atmospheric Pressure Ionization Mass Spectrometry (APIMS), J. Geophys. Res. Atmos., doi:10.1029/2002JD002289, 2002a.

Thornton, J. A., Wooldridge, P. J. and Cohen, R. C.: Atmospheric NO 2 : In Situ Laser-Induced Fluorescence Detection at

835 Parts per Trillion Mixing Ratios , Anal. Chem., 72(3), 528–539, doi:10.1021/ac9908905, 2002b.

Tuovinen, J. P., Ashmore, M. R., Emberson, L. D. and Simpson, D.: Testing and improving the EMEP ozone deposition module, in Atmospheric Environment., 2004.

Veres, P., Roberts, J. M., Warneke, C., Welsh-Bon, D., Zahniser, M., Herndon, S., Fall, R. and de Gouw, J.: Development of negative-ion proton-transfer chemical-ionization mass spectrometry (NI-PT-CIMS) for the measurement of gas-phase organic

840 acids in the atmosphere, Int. J. Mass Spectrom., 274(1–3), 48–55, doi:10.1016/j.ijms.2008.04.032, 2008.

Vermeuel, M. P., Novak, G. A., Alwe, H. D., Hughes, D. D., Kaleel, R., Dickens, A. F., Kenski, D., Czarnetzki, A. C., Stone, E. A., Stanier, C. O., Pierce, R. B., Millet, D. B. and Bertram, T. H.: Sensitivity of Ozone Production to NOx and VOC Along the Lake Michigan Coastline, J. Geophys. Res. Atmos., 124(20), 10989–11006, doi:10.1029/2019JD030842, 2019.

Voisin, D., Smith, J. N., Sakurai, H., McMurry, P. H. and Eisele, F. L.: Thermal desorption chemical ionization mass

845 spectrometer   for   ultrafine   particle   chemical   composition,   Aerosol   Sci.   Technol.,   37(6),   471–475, doi:10.1080/02786820300959, 2003.

Webb, E. K., Pearman, G. I. and Leuning, R.: Correction of flux measurements for density effects due to heat and water vapour transfer, Q. J. Roy. Meteorol. Soc., 106(447), 85–100, doi:http://dx.doi.org/10.1002/qj.49710644707, 1980.

Weinheimer, A. J.: Chemical Methods: Chemiluminscence, Chemical Amplification, Electrochemistry, and Derivation, in

850 Analytical Techniques for Atmospheric Measurement., 2007.

Werle, P., Miicke, R. and Slemr, F.: The Limits of Signal Averaging in Atmospheric Trace-Gas Monitoring by Tunable Diode-Laser Absorption Spectroscopy (TDLAS), , 139, 131–139, 1993.

Wesely, M. L. and Hicks, B. B.: A review of the current status of knowledge on dry deposition, Atmos. Environ.,

doi:10.1016/S1352-2310(99)00467-7, 2000.

855 Wesely, M. L., Cook, D. R. and Williams, R. M.: Field measurement of small ozone fluxes to snow, wet bare soil, and lake water, Boundary-Layer Meteorol., 20(4), 459–471, doi:10.1007/BF00122295, 1981.

Wienhold, F. G., Welling, M. and Harris, G. W.: Micrometeorological measurement and source region analysis of nitrous oxide fluxes from an agricultural soil, Atmos. Environ., 29(17), 2219–2227, doi:10.1016/1352-2310(95)00165-U, 1995.

Wilczak, J. M., Oncley, S. P. and Stage, S. A.: Sonic anemometer tilt correction algorithms, Boundary-Layer Meteorol., 99(1),

860 127–150, doi:10.1023/a:1018966204465, 2001.

Wolfe, G. M., Hanisco, T. F., Arkinson, H. L., Bui, T. P., Crounse, J. D., Dean-Day, J., Goldstein, A., Guenther, A., Hall, S. R., Huey, G., Jacob, D. J., Karl, T., Kim, P. S., Liu, X., Marvin, M. R., Mikoviny, T., Misztal, P. K., Nguyen, T. B., Peischl, J., Pollack, I., Ryerson, T., St. Clair, J. M., Teng, A., Travis, K. R., Ullmann, K., Wennberg, P. O. and Wisthaler, A.: Quantifying sources and sinks of reactive gases in the lower atmosphere using airborne flux observations, Geophys. Res. Lett.,

865 42(19), 8231–8240, doi:10.1002/2015gl065839, 2015.

Yang, M., Beale, R., Smyth, T. and Blomquist, B.: Measurements of OVOC fluxes by eddy covariance using a proton-transfer-reaction mass spectrometer-method development at a coastal site, Atmos. Chem. Phys., 13(13), 6165–6184, doi:10.5194/acp-13-6165-2013, 2013.

Yang, M., Prytherch, J., Kozlova, E., Yelland, M. J., Parenkat Mony, D. and Bell, T. G.: Comparison of two closed-path cavity-

870 based spectrometers for measuring air-water CO_2 and CH_4 fluxes by eddy covariance, Atmos. Meas. Tech., 9(11), 5509–5522, doi:10.5194/amt-9-5509-2016, 2016.

Yienger, J. J. and Levy, H.: Empirical model of global soil-biogenic NO χ emissions , J. Geophys. Res., doi:10.1029/95jd00370, 2004.

Zafiriou, O. C. and McFarland, M.: Nitric oxide from nitrite photolysis in the central equatorial Pacific., J. Geophys. Res.,

875 86(C4), 3173–3182, doi:10.1029/JC086iC04p03173, 1981.

Zahn, A., Weppner, J., Widmann, H., Schlote-Holubek, K., Burger, B., Kühner, T. and Franke, H.: A fast and precise chemiluminescence ozone detector for eddy flux and airborne application, Atmos. Meas. Tech., 5(2), 363–375, doi:10.5194/amt-5-363-2012, 2012.

Zhang, L., Brook, J. R. and Vet, R.: A revised parameterization for gaseous dry deposition in air-quality models, Atmos. Chem.

880 Phys., doi:10.5194/acp-3-2067-2003, 2003.

885

890

895

900

905

Species	Normalized Sensitivity (8 g kg^{-1} SH, 1σ)	Absolute Sensitivity (8 g kg^{-1} SH)	LOD optimum	LOD (1 Hz)	LOD (10 Hz)	Background (cps, 1σ)	Precision (10 Hz)	Field Calibration R^2
O$_3$	12.4 ± 1.2 ncps pptv^{-1}	180 cps pptv^{-1}	4.0 pptv (11s)	13 pptv	42 pptv	3.1 x 10^5 ± 5.0 x 10^4	0.74%	0.99
NO$_2$	6.7 ± 1.0 ncps pptv^{-1}	97 cps pptv^{-1}	2.3 pptv (19s)	9.9 pptv	32 pptv	5.1 x 10^4 ± 1 x 10^4	1.1%	— — —

910 **Table 1. Summary of instrument sensitivity, precision, and accuracy for detection of O$_3$ and NO$_2$ from laboratory calibrations. Sensitivity is reported at a specific humidity (SH) of 8 g kg^{-1} which corresponds to 40% RH at 25 °C. All limits of detection (LOD) are for a S/N = 3. The optimum LOD is reported as the LOD at the optimum averaging time determined by the minimum of the Allan variance spectrum. Optimum averaging times were determined to be 11 s for O$_3$ and 19 s for NO$_2$. The reported field comparison (R^2) is from a regression of 1-minute bin averaged ozone concentration from the Ox-CIMS with an EPA (Thermo-Fisher**
915 **49i) monitor in Zion, Il during four weeks of ambient observation shown in Fig. 7.**

920

925

930

935

Species	Concentration Mean (ppb) & 1σ range	5th to 95th percentile Concentration Range (ppbv)	v_d mean (cm s^{-1})	v_d 20-80% range (cm s^{-1})	v_d LOD 1.96σ (cm s^{-1})
O$_3$	41.2± 10.1	28.9 – 67.1	0.013	-0.0011 – 0.027	0.0027
NO$_2$	4.7 ± 5.5	0.45-16.9	----------	----------	----------

Table 2. Overview of flux and concentration measurements of O$_3$ and NO$_2$ from Scripps Pier. Concentration ranges are reported for all periods of onshore winds. Flux results are reported only for final quality-controlled flux periods Ozone mean deposition velocity (v_d) was well resolved from the campaign ensemble average LOD of 0.0042 cm s^{-1}. Reported v_d LOD is the ensemble mean of the LOD determined by the RMSE method at long lag times for each 27-minute flux period. 39% of quality-controlled flux periods fell below the campaign ensemble LOD. Deposition velocity of NO$_2$ across the air-sea interface is expected to be small (<0.002 cm s^{-1}) and was consistently below the LOD of our instrument so no values are reported here.

940

945

950
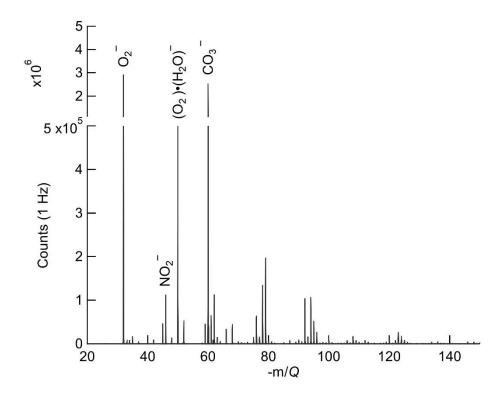
Figure 1: Ox-CIMS mass spectra collected at 1 Hz and mass resolution of 950 $M/\Delta M$ **(at −60 m/Q), with major peaks highlighted.** O_2^- **and** $O_2(H_2O)^-$ **at −32 m/Q and −50 m/Q respectively are the two observed forms of the reagent ion. The detected ozone product**
955 **(CO_3^-, −60 m/Q) is of comparable magnitude to the** O_2^- **reagent ion during ambient sampling. NO_2 is detected as the charge transfer product** NO_2^- **at −46 m/Q. Masses greater than −150 m/Q contribute less than 2% to the total signal and are not plotted.**

960

965
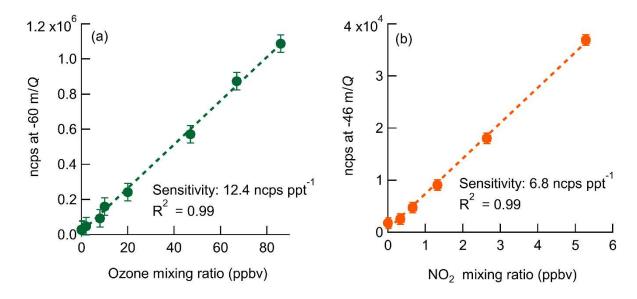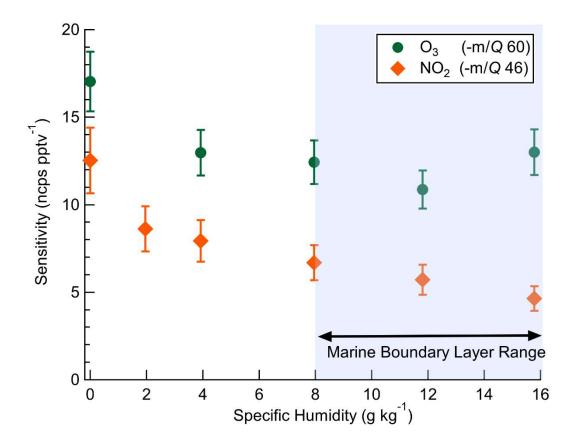
970 **Figure 2: Normalized calibration curves of O₃ (a) and NO₂ (right) at 8 g kg⁻¹ specific humidity (approximately 40% RH at 25 °C). Ozone is detected as CO₃⁻ at –60 m/Q. NO₂ is detected as the charge transfer product (NO₂⁻) at –46 m/Q. Error bars are the standard deviation in normalized count rate for each measurement point.**

975 **Figure 3: Dependence of O₃ and NO₂ sensitivities on specific humidity. Error bars indicate standard deviation of triplicate calibration curves. The blue shaded region from SH 8–16 g kg⁻¹ is the approximate typical range of specific humidity in the mid-latitude marine boundary layer.**
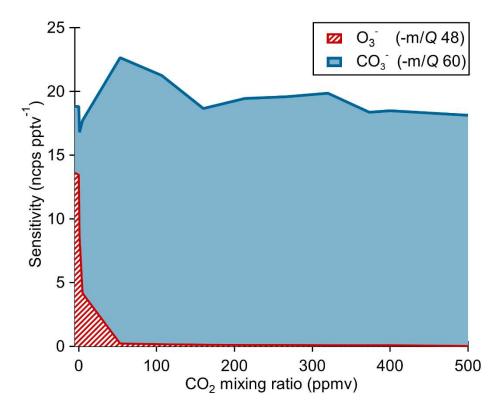
980   **Figure 4: Ox-CIMS cumulative sensitivity to O₃ detected either directly as O_3^- or as CO_3^- as a function of CO₂ mixing ratio. The sum of sensitivity as O_3^- and CO_3^- shows that total sensitivity to O₃ is conserved as the product distribution shifts with CO₂ mixing ratio. Greater than 99% of O3 is observed as CO_3^- at CO₂ mixing ratios greater than 60 ppmv.**
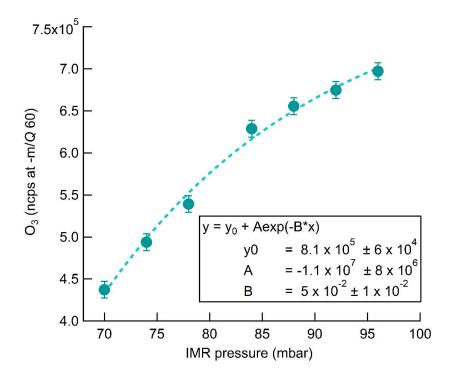
Figure 5. Normalized count rate of CO_3^- (–60 m/Q) ozone detection product as a function of pressure in the IMR during sampling of a constant 35 ppbv O_3 source. The exponential fit of the data is shown by the dashed line. Fit parameters are included to allow for calculation of potential sensitivity improvements with further increase in IMR pressure.

985
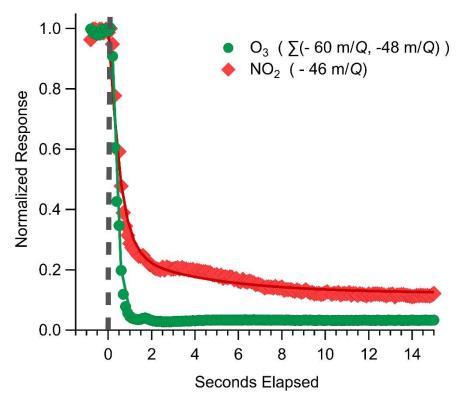
Figure 6: Representative instrument backgrounding determination for O₃ and NO₂ where the inlet was rapidly switched from ambient sampling to an overflow with dry UHP N₂ indicated by the grey dashed line. O₃ response is fit to anexponential decay, plotted as solid lines with a mean response time of 0.28 s.,NO₂ is fit to a bi-exponential decay where the initial rapid decay (τ_1) in attributed to gas evacuation of the inlet line and the second slower decay (τ_2) is attributed to equilibration with the inlet walls. Best fit estimates for τ_1 of NO₂ from 0.7 to 1.2 seconds. τ_2 for NO₂ was determined to be 3.2 s for this decay period.

990

995
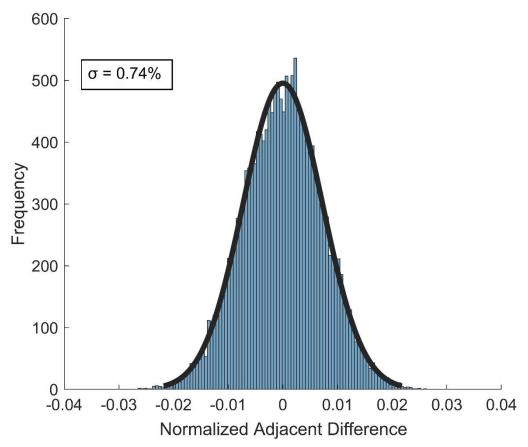
Figure 7: Distribution of normalized adjacent differences measured at 10 Hz during a stable 27-minute ambient sampling period of 38 ppbv O$_3$ from Scripps Pier. The 1σ value of the distribution gives an upper limit of instrument precision of 0.74%.

1000
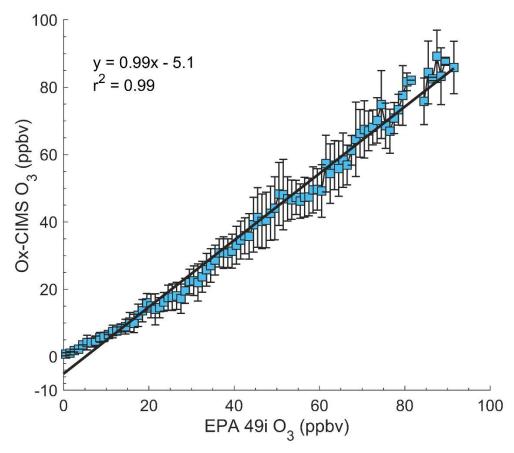
1005 **Figure 8: Regression of 1-minute average O_3 mixing ratios from the Ox-CIMS against an EPA O_3 monitor (Thermo-Fisher 49i) binned to 1 ppbv over four weeks of ambient sampling in Zion, Illinois in May- June 2017. The solid black line is the linear least-squares regression. Error bars represent the standard deviation of each bin. Instrument agreement is strong for O_3 greater than 10 ppbv, with an apparent bias in one or both instruments below 10 ppbv.**

1010
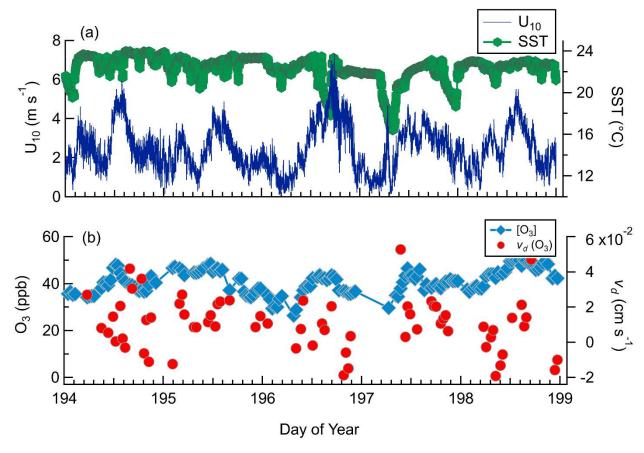
Figure 9: Observed meteorology and O₃ mixing ratio and deposition velocities for DOY 194-199 from Scripps Pier (a) Horizontal wind speed (U₁₀) and sea-surface temperature (SST). (b) O₃ mixing ratios and v_d(O₃).
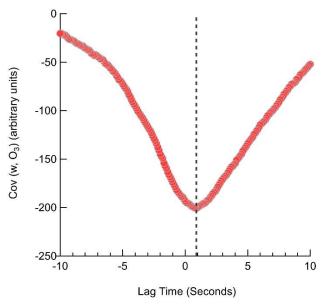
1015 **Figure 10: Lag time determination for an individual 27-minute O$_3$ flux averaging period. The lag time for this flux period determined from the maximum of the covariance to be 0.9 seconds which compares reasonably with the volumetric evacuation time of the inlet of 1.7 to 2.1 seconds.**

1020

1025
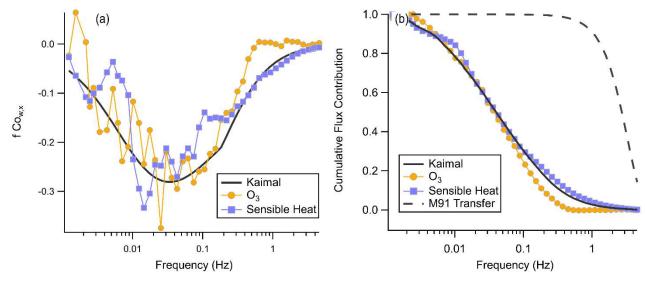
Figure 11. (a) Mean binned frequency weighted cospectra O₃ and sensible heat flux with vertical wind from the average of two consecutive flux periods from 14:10 – 15:20 local time on July 20th. The Kaimal trace is the idealized cospectra Kaimal et al. (1972) for mean windspeed of 4.4 m s⁻¹ and an unstable atmosphere. The sensible heat trace is inverted, and the observed net sensible heat flux was positive for this period (b) Corresponding ogives for cospectra shown in (a). The M91 Transfer trace is the calculated
1030 **transfer function for turbulent attenuation in a tube from (Massman, 1991).**

1035
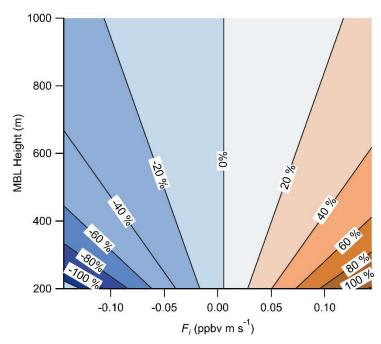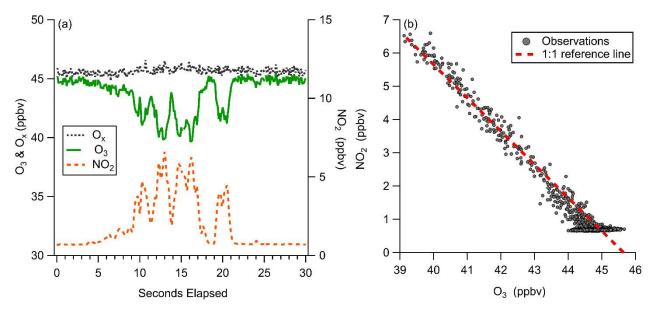
Figure 12. Calculated percent error in the measured O₃ surface flux due to entrainment from the free troposphere as a function of the MBL height and the entrainment flux (F_i). Entrainment flux is the product of the free troposphere to boundary layer concentration gradient (ΔC), and the entrainment velocity (w_e). Calculation of percent error used the Scripps Pier measuring height of 13 m, and mean surface flux of -5.6 x 10⁻³ ppbv m s⁻¹.

Figure 13: Observations of ozone titration by NO emissions from a boat engine near the SIO pier. (a) 10 Hz timeseries of O_3, NO_2, and O_x (O_3 + NO_2) demonstrating ability to capture transient titration events. (b) Regression of O_3 and NO_2 plotted with a reference line of slope -1, showing conservation of total O_x at 10 Hz during a NO titration event.

1050

1055

1060